RSC Advances

REVIEW

View Article Online
View Journal | View Issue

Cite this: *RSC Adv.*, 2025, **15**, 11587

Iron oxide based magnetic nanoparticles for hyperthermia, MRI and drug delivery applications: a review

Rizwana Ghazi,[a] Talib K. Ibrahim,[bc] Jamal Abdul Nasir,[a] Shili Gai,[d] Ghafar Ali,[e] Imed Boukhris[f] and Ziaur Rehman*[a]

Received 31st January 2025
Accepted 24th March 2025

DOI: 10.1039/d5ra00728c

rsc.li/rsc-advances

Iron-oxide nanoparticles (IONPs) have garnered substantial attention in both research and technological domains due to their exceptional chemical and physical properties. These nanoparticles have mitigated the adverse effects of conventional treatment procedures by facilitating advanced theranostic approaches in integration with biomedicine. These IONPs have been extensively utilized in MRI (as contrast agents in diagnosis), drug delivery (as drug carriers), and hyperthermia (treatment), demonstrating promising results with potential for further enhancement. This study elucidates the operational principles of these NPs during diagnosis, drug delivery, and treatment, and emphasizes their precision and efficacy in transporting therapeutic agents to targeted sites without drug loss. It also analyses various challenges associated with the application of these IONPs in this field, such as biocompatibility, agglomeration, and toxicity. Furthermore, diverse strategies have been delineated to address these challenges. Overall, this review provides a comprehensive overview of the applications of IONPs in the field of biomedicine and treatment, along with the associated challenges. It offers significant assistance to researchers, professionals, and clinicians in the field of biomedicine.

1 Introduction

With the rapid development of nanotechnology, nanoparticles (NPs) have garnered significant attention over bulk materials owing to their unique properties including tunable shapes, sizes, high surface areas, biocompatibility, and superparamagnetism. These properties facilitate their applications in diverse fields.[1–3] Nanomedicine is an integral component of biotechnology and plays a crucial role in diagnostics and drug delivery.[4] IONPs have been extensively investigated as nanomedicines for the diagnosis and treatment of tumor cells because of their high saturation magnetization (M_s) values and easy functionalization.[5] For instance, the M_s value for IONPs with a large particle size (45 nm) has been reported to be 92 emu, which is greater than that of IONPs with a small particle size (20 nm) with an M_s value of 80 emu.[6] This shows an inverse relationship between the size of the NPs and their M_s values, which is attributed to the reduced surface area effect.[7] Functionalization of IONPs plays a crucial role in tailoring their properties for specific applications. While various strategies exist for surface modification, the choice of functionalization method should be carefully considered based on the intended application and potential biological impacts. Furthermore, M_s also depends on various other factors such as the synthesis procedure, surface chemistry, and chemical nature of the compound. Superparamagnetic IONPs (SPIONPs) have also been used for the diagnosis and treatment of cancer cells.[8]

IONPs have been widely reported for biomedical applications, such as contrast agents in magnetic resonance imaging (MRI), nanoplatforms for targeted drug delivery, cell labeling, and magnetic hyperthermia for the treatment of cancer cells.[9] However, these NPs face the challenges of limited biocompatibility and toxicity, posing serious risks to biosystems upon exposure.[5,10,11] These issues have been addressed through surface modification and composite formation with other agents such as polymers (chitosan,[12,13] dextran,[14–16] polyethylene glycol,[17,18] poly lactic *co*-glycolic acid (PLGA),[19,20] and polyvinyl alcohol).[21,22] Known examples of ferrite-based composites are carboxymethyl dextran-coated Mn–Zn ferrite,[23] polyethylene-coated Ni-ferrite,[24,25] chitosan-coated Fe_3O_4,[26,27] Ni–Zn ferrite using glycine, oleic acid-coated Fe_3O_4.[28,29] These coating agents reduce the agglomeration of IONPs and decrease their likelihood of recognition by the immune system, thereby improving

---

[a] *Department of Chemistry, Quaid-i-Azam University, Islamabad 45320, Pakistan. E-mail: zrehman@qau.edu.pk; Fax: +92-(051)90642241; Tel: +92-(051)90642245*

[b] *Department of Petroleum Engineering, College of Engineering, Knowledge University, Erbil, Iraq*

[c] *Department of Petroleum Engineering, Al-Kitab University, Altun Kupri, Iraq*

[d] *Key Laboratory of Superlight Materials and Surface Technology, Ministry of Education, College of Materials Science and Chemical Engineering, Harbin Engineering University, Harbin, 150001, P. R. China*

[e] *Nanomaterials Research Group (NRG), Physics Division, PINSTECH, Nilore, Islamabad, Pakistan*

[f] *Department of Physics, Faculty of Science, King Khalid University, P. O. Box 9004, Abha, Saudi Arabia*

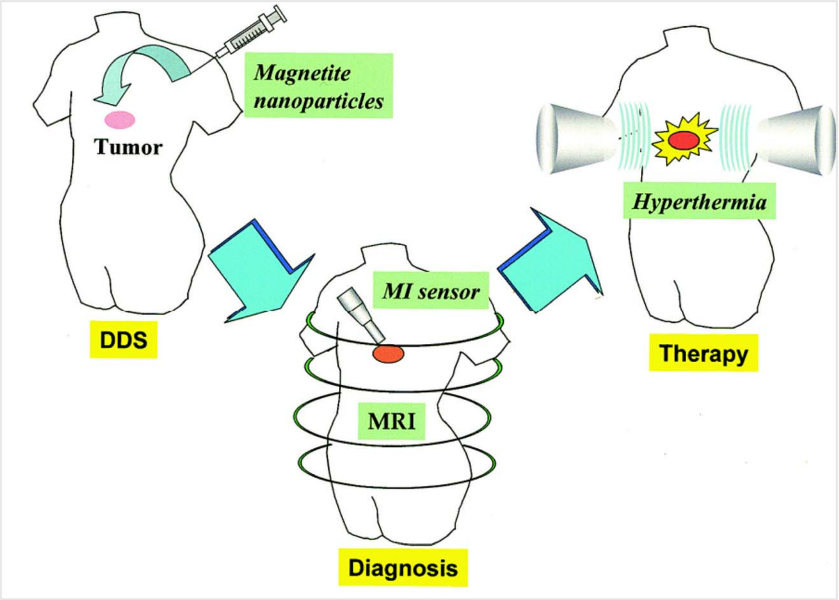

Fig. 1 Biomedical applications of IONPs. Copyright 2005, Elsevier.[36]

their bio-interactions.[30] Moreover, the size of NPs plays a significant role in addressing biocompatibility and toxicity issues.

Several nanomedicines, which are combinations of organic compounds incorporated into IONPs, have already been approved by the United States Food and Drug Administration (USFDA) and the European Medicine Agency (UMA) for preclinical and clinical trials. However, most of these drugs were rejected after preclinical trials for the aforementioned reasons. Cancer is one of the deadliest diseases in the world ever faced. It has led to the second-highest mortality rate globally, and this rate is projected to increase in the future.[31,32] Therefore, timely diagnosis and treatment are major concerns in this regard.[33] In recent years, the transportation of nanodrug carriers to targeted sites has remained a challenge, resulting in the insufficient delivery of drug doses that are inadequate for cancer treatment. Consequently, IONPs have emerged as potential candidates for overcoming the challenges related to the efficacy of therapeutic drugs.[34,35]

This review discusses the major biomedical applications of IONPs in the field of biomedicine, such as contrast agents in MRI, as drug carriers in targeted drug delivery, and heat dissipation in hyperthermia. The operating principle of these IONPs is also discussed in detail for each application. The various biomedical applications of magnetic IONPs are shown in Fig. 1.

2. Magnetic resonance imaging

The discovery of Magnetic Resonance Imaging (MRI) is credited to two physicists, Felix Bloch and Edward Mills Purcell, who independently described this phenomenon in 1947.[37] MRI operates based on the principles of nuclear magnetic resonance (NMR).[38–40] In contrast to other imaging techniques such as CT scans, MRI stands out as a non-invasive method that avoids the use of ionizing radiation and produces high-quality images of soft tissues. However, there are certain limitations, such as high cost and the need for stagnation of patients during the imaging process.[41]

Molecular Imaging (MI) has garnered substantial interest owing to its capacity to merge molecular biology with *in vivo* imaging, enabling analyses and diagnoses at molecular and cellular levels.[42] It enables early disease detection, notably cancer, aids therapy response assessment, and delves into live-subject biological processes. Once administered into the body MRI, PET, CT, and ultrasound are the main *in vivo* imaging modalities, with MRI being the most versatile in providing both functional and anatomical information with excellent image quality and using non-ionizing radiation, allowing for longitudinal studies without side effects.[43] Chen *et al.*[44] developed physiologically stable nanoconjugates of IONPs by encapsulating and functionalizing them with triblock copolymer and IRDye800/RGD peptide respectively. These nanoconjugates were subsequently investigated for *in vivo* MR images using a U87MG xenografted tumor model. The pharmacokinetics were thoroughly examined, and they were found to exhibit excellent tumor targeting capabilities. The polymer coating contributed to conferring stability while resisting opsonization. In another study, Hachani *et al.*[45] reported IONPs functionalized with 3,4-dihydroxyhydrocinnamic acid (DHCA) as a T_2-contrast agent. The modified IONPs were interacted with human mesenchymal stem cells (hMSCs), and various parameters were evaluated, such as mitochondrial health and cell viability studies. These studies demonstrated that cell labeling with modified IONPs had minimal effect on hMSCs. Thus *in vivo* studies, the modified IONPs produce enhanced T_2 contrast effect and are potential contrast agents for stem cell tracking by T_2-weighted MRI as they show no evidence of cytotoxic effects on hMSCs.

Similarly, non-cytotoxic material, PEG, was employed for coating Mn-IONPs to enhance biocompatibility, and the resulting IONPs were studied as dual contrast agents for *in vivo* imaging using CCK-8 analysis. Significant alteration in the signal ratio was observed Xiao *et al.*,[46] for both T_1 and T_2, which certainly originated due to the *in vivo* distribution of the IONPs. After accumulating in the liver within a short interval of 10 min, a greater T_2 contrast enhancement was observed as compared to T_1, which is attributed to the cluster formation of the contrast agents as a result of passive aggregation from Kupffer cell phagocytosis. The *in vivo* MRI results confirmed that these NPs function as highly sensitive dual contrast agents (T_1 and T_2) for liver imaging. PEG-Arg@IONPs were administered to murine subjects and analyzed utilizing MRI techniques by Nosrati *et al.*[47] This investigation examined the biocompatibility and biodegradation of IONPs. The findings revealed minimal hepatic accumulation in the early stages and extended circulation time of IONPs. This study presents the first instance of employing MRI for a stereological investigation of IONPs to assess biocompatibility, monitor biodegradation, and track distribution. MRI techniques were utilized at intervals to evaluate the cardiac, renal, hepatic, and splenic tissues, validating biodegradation and clearance from body organs. The PEG-Arg@IONPs investigated demonstrate potential as T_2 contrast agents for imaging target organs.

Vascular endothelial growth factor (VEGF) plays a critical role in cancer development and progression. A multifunctional VEGF-targeted molecular imaging probe was developed by Lin *et al.*[48] using NIR830 labeled bevacizumab encapsulated IONPs for optical and MR imaging of VEGF-overexpressing 4T1 breast tumor cells in mice. Bevacizumab (Avastin®), which targets VEGF and inhibits angiogenesis, served as the targeting ligand. The targeting efficacy was evaluated through receptor-mediated cell uptake experiments and blocking assay administration resulting in enhanced accumulation in tumors compared to non-targeted IONPs. Quantitative analysis of T_2-weighted MRI 48 hours post-injection revealed that the average percentage of signal intensity change in tumors treated with NIR830-bevacizumab-IONPs was 52.4 ± 11.0%, in contrast to 26.9 ± 12.4% in controls treated with non-targeted IONPs. Furthermore, for a comprehensive review of *in vivo* studies on reported IONPs-based nanocomposites, a detailed review article is available in the literature. In this article, Lamichhane *et al.* examined the potential toxicity issues associated with IONPs-based contrast agents and the corresponding challenges in their clinical trials.[49]

The properties of IONPs can be tuned for use as MRI contrast agents by controlling their saturation magnetization and magnetic anisotropy. As compared to ferrimagnetic materials, the superparamagnetic iron oxides show potential magnetic susceptibility for application as contrast agent while showing almost no remanent magnetization after the removal of the external magnetic field. This property makes them ideal for application as contrast agents in MRI, as shown in Fig. 2. Once administered into the body, the contrast agents bind to molecules at the targeted site through bioligands, thereby shortening the time it takes for protons to align with the magnetic field.[51] The interaction of relaxation processes with water molecules in the body further enhances the signals produced. Brighter MR images can be obtained by shortening the time taken for realignment.[52–56] T_2 sequences generally produce brighter MR images evident from literature.[57]

The size of IONPs has a significant positive or negative impact on their magnetic behavior below certain limits.[58–60] Fig. 3(a and b) illustrates the dependence of magnetization on the size and associated coercivity of magnetic nanoparticles.

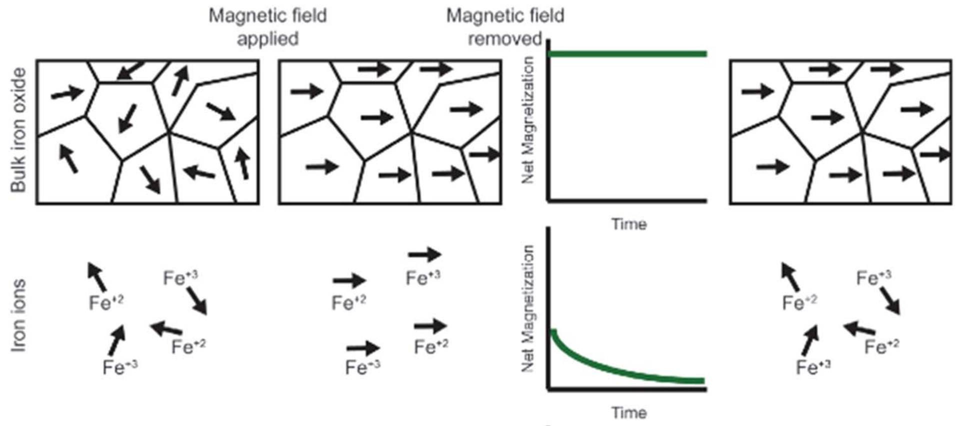

Fig. 2 Effect of external magnetic field on the net magnetization of bulk magnetite, iron ions, and SPIONs. Copyright 2011, Elsevier.[50]

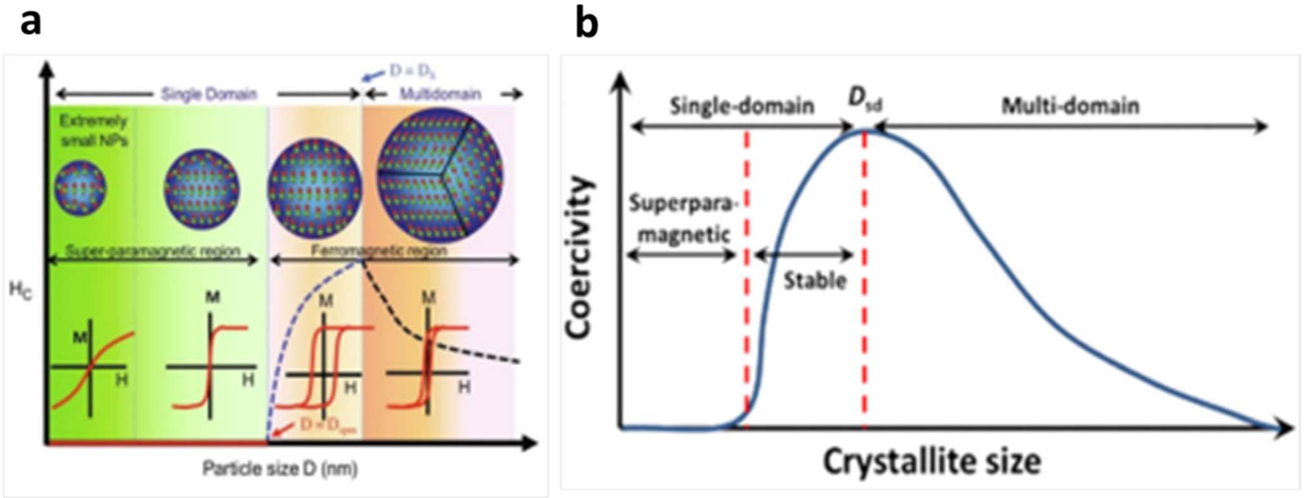

Fig. 3 (a and b) Dependence of magnetization on size of IONPs. Copyright 2005 & 2018, Elsevier.[58,59]

Over the last two decades, numerous studies have aimed to develop IONPs to enhance the diagnosis and treatment of various diseases. IONPs are the most extensively studied MNPs as contrast agents in MRI owing to their superparamagnetic properties. The enhanced surface area offered by these NPs allow for easy interaction and modification with coating agents such as polymers. The superparamagnetic property also allows the NPs to be attracted to the external magnetic field and directly transferred to the desired site without causing significant damage to the healthy tissues ultimately enhancing their biocompatibility.[58,61]

2.1 Principle of MRI: image contrast

MRI works on the principle of NMR, where a patient or sample is placed under the influence of a magnetic field, resulting in magnetic resonance signals.[62] MRI uses the magnetic properties of hydrogen atoms to generate detailed images of the body. When a primary magnetic field is applied, the hydrogen atoms align their spin parallel or anti-parallel to the field, producing longitudinal magnetization. Gradient coils inside the bore of the MRI machine produce a secondary magnetic field, changing the precessional frequency of the nuclei and enabling 3D imaging. The radiofrequency coil transmits radio waves that excite the nuclei and causes them to absorb energy, moving to a higher energy state. After radiofrequency is turned off, the nuclei undergo relaxation and return to equilibrium, releasing the energy detected by the MRI machine (Fig. 4).[63]

The precessional frequency causes protons to spin in an in-phase manner, changing the longitudinal magnetization into transverse magnetization. The strength of the magnetic field affects the sensitivity and spatial resolution of MRI, with stronger fields producing more intense radiofrequency radiation and higher spatial resolution. However, excessive absorption of radiofrequency radiation elevates the body temperature above normal levels, so in clinics, MRI currently uses magnetic field intensities of 1.5–3.0 T.[56]

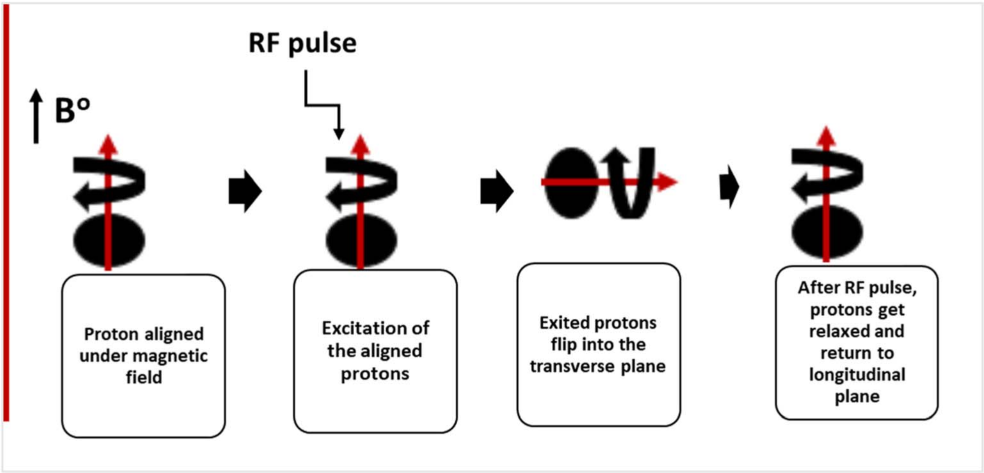

Fig. 4 Working principle of MRI.

2.2 Relaxation processes

There are two types of relaxation processes: T_1 and T_2 relaxation. When protons relax and retain their low energy state before radiofrequency radiation is emitted, the induced magnetization is called longitudinal magnetization (T_1) and is always parallel to the primary magnetization. Longitudinal magnetization is also known as spin-lattice magnetization. On the other hand, the magnetization caused by flipping the protons to higher energy is called inverse magnetization (T_2). It is always perpendicular to the primary magnetization and is also called spin–spin relaxation. Both T_1 and T_2 relaxations depend on the composition of tissues; for instance, the T_1 relaxation for water is slow due to the quick movement of water molecules and does not flip to a low-energy state quickly; however, the T_2 relaxation for water is comparatively quick.[56]

The tissues under observation inherently have a characteristic number of protons that respond to the magnetic field and undergo rotational processes. Thus, the associated relaxation time is characteristic of the tissue environment, and normally, the given proton density does not sufficiently produce contrast in clinical MR scanning.[64] Therefore, contrast agents are administered in the body prior to MRI to vary the fixed relaxation time and magnetic behavior of the neighboring protons, ensuring quality MR imaging. The r_1 ($1/T_1$) and r_2 ($1/T_2$) relaxation times are related to the rate of recovery of longitudinal magnetization and the decay rate of transverse magnetization. Therefore, T_1 contrast agents with shorter T_1 relaxation times appear as brighter images; however, T_2 contrast agents with shorter T_2 relaxation times appear dark due to the rapid loss of transverse magnetization as they decay during the process.[65,66] The mechanisms of T_1 and T_2 relaxation are shown in Fig. 5.

Regarding the particle size effect, Brooks *et al.*[68] stated that with the increased size of NPs, r_2 relaxivity and magnetization increase. After reaching an optimum size, the relaxation process no longer becomes dependent on diffusion and is not affected by a further increase in size. Another strategy to enhance the magnetic properties of MRI is to produce small nanocluster IONPs to increase the magnetic size. Chen and co-workers[69] have established a NPs cluster using amphiphilic block copolymer which increased the high transverse relaxivity (r_2 value).

2.3 Types of contrast agents

2.3.1 T_1 contrast agents. The first generation of exogenous T_1 contrast agents, which produce hyperintense signals in T_1-weighted images, consists of high-spin paramagnetic metal ions such as manganese (Mn^{2+}),[70] iron (Fe^{3+}),[71] or gadolinium (Gd^{3+}).[65] However, these cations are toxic and can harm professional macrophages by displacing endogenous calcium ions.[72,73] To prevent this toxicity, low-molecular-weight chelating molecules are employed to create stable complexes with ions. Gd is the most clinically used metal ion in paramagnetic T_1 contrast agents and is complexed with chelating compounds, such as diethylene-triamine-pentaacetic acid (DTPA), dipyridoxyl-di-phosphate (DPDP), and 1,4,7,10-tetraazacyclo-dodecane-1,4,7,10-tetraacetic acid (DOTA). T_1 agents are neutral or anionic metal complexes with macrocyclic or acyclic polyaminopolycarboxylate structures. Various Gd-containing contrast agents have been approved for MRI use by regulatory agencies such as the European Medicines Agency (EMA) and the US Food and Drug Administration (FDA).[74,75]

Gadolinium (Gd), when used as a chelated compound, is generally considered safe owing to its versatile imaging capabilities. However, it is essential to be aware that certain Gd chelates have been associated with a rare, yet severe complication called nephrogenic systemic fibrosis (NSF), which is primarily observed in patients with renal conditions. Consequently, the World Health Organization (WHO) has implemented restrictions on the use of Gd contrast agents. These limitations apply to patients with chronic severe renal insufficiency, individuals experiencing acute renal insufficiency due to hepatorenal syndrome, those undergoing perioperative liver transplantation, and newborns under four weeks of age.[75]

The drawbacks of conventional Gd-based contrast agents stem from their low molecular weight and rapid extravasation from the vascular space, leading to a partial-volume dilution effect. Extracellular agents, which constitute the predominant

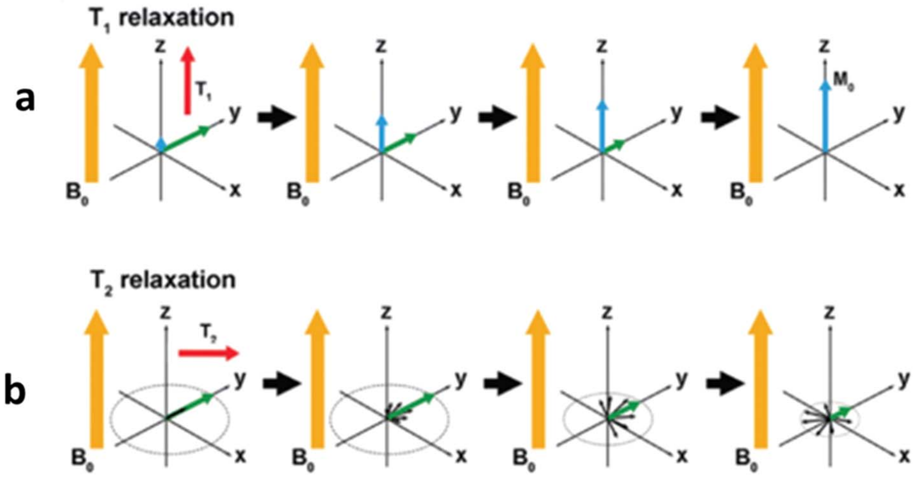

Fig. 5 Mechanism of T_1 relaxation and T_2 relation[67]

class of MRI contrast agents, typically comprise Gd chelates featuring linear or macrocyclic polyaminocarboxylate ligands. Efforts to enhance MRI by directly attaching Gd ions to antibodies or proteins have proven to be inadequate for effectively reducing local relaxation times and delivering significant MR signal enhancement. In specialized applications such as MR angiography, specific contrast agents must function as blood-pool agents, characterized by their high molecular weight and enhanced relaxivity. These attributes hinder diffusion across the vascular epithelium and interstitial leakage, thereby allowing prolonged residence within the vascular system. Noteworthy examples of blood-pool agents include Gd-based complexes that interact noncovalently with human serum albumin and Gd chelates bound to polymers.[76–78]

Mn-based NPs have been investigated as alternatives to Gd-based contrast agents. These NPs have the advantage of a longer circulation time and potentially greater specificity for targeting precise tissues.[76] However, their clinical use is still in the early stages of development and requires further investigation. It is important to note that Mn-based contrast agents have their own potential risks and limitations. Mn is an essential nutrient in small amounts; however, excessive exposure to Mn can lead to toxicity, particularly in the brain. Studies have suggested that long-term exposure to high levels of Mn in the workplace may cause a condition called manganism, which shares symptoms with Parkinson's diseases.[79] Mn-based contrast agents are being investigated as alternatives to the most widely used Gd-based contrast agents; however, their clinical use requires further investigation and monitoring of potential risks.[76,80]

Passive targeting is mainly based on enhanced permeability effect which was initially described by Prof. Maeda in 1986, is referred to as the Enhanced Permeability and Retention (EPR) effect.[81] It is a process observed in solid tumors where NPs and macromolecules can accumulate selectively at tumor site due to its abnormal vasculature. The EPR effect is based on two key features of tumor biology: increased vascular permeability and impaired lymphatic drainage. The leaky structure and gaps between the epithelial tumor cells cause the IONPs to easily extravasate and retain in the tumor interstitium for longer time.[82,83] However, this phenomenon is not universal and depends on various factors such as physical characteristics of patient, type and location of tumor *etc.* For instance, in glioblastoma treatment, the presence of the blood–brain barrier (BBB) and blood–brain tumor barrier (BBTB), poses significant challenges to EPR which relies on the passive accumulation of IONPs in tumors owing to leaky vasculature.[83,84]

Several studies have reported tumor accumulation of IONPs *via* the EPR effect, ranging from 5% to 21.7% of the injected dose per gram of tissue (ID/g). For instance, Biancacci *et al.* reported tumor accumulation increasing from 7% to 15% ID per g during treatment,[85] while Goos *et al.* showed exceptionally high uptake of 14.8–21.7% ID per g in tumors with high EPR characteristics. However, the papers also highlighted significant variability in the EPR effect.[86] Lee *et al.* reported a 35-fold variation in tumor accumulation (0.52–18.5% ID per kg) in clinical studies, indicating high heterogeneity.[87] Nevertheless, it is recognized that the EPR effect's intensity varies based on factors such as tumor type, stage of development, and the heterogeneity of blood vessels.[88] Future research should focus on better understanding and exploiting the EPR effect to improve the efficacy of contrast agents and nanomedicines in cancer imaging and therapy.

The undermentioned are the factors affecting the efficiency of T_1 contrast agents.

2.3.1.1. *Size of contrast agent.* Magnetization of IONPs depends mainly on their sizes; therefore, the strength of the contrast effect changes significantly with variations in the size of IONPs.[59] The T_1 contrast effect can be enhanced by reducing the size of the IONPs. This is because an increase in the spin-canted layer of the IONPs occurs. However, it is still comparatively smaller than that of normal superparamagnetic NPs and possesses an enhanced T_1 contrast effect than T_2.[89,90] Usually, both r_1 and r_2 relaxivities decrease with a decrease in the size of the contrast agents; nevertheless, unlike r_1, r_2 is also mainly dependent on the magnetic moment. Therefore, r_2 contributes more than r_1 to the reduction of the r_2/r_1 ratio.[90]

2.3.1.2. *Surface state of contrast agent.* To increase biocompatibility and deter the agglomeration of IONPs, certain coating agents are normally employed. Coating not only alters the surface properties of the IONPs, but also has an impact on the T_1 contrast effect.[91] T_1 contrast effect is affected by the thickness of the coating agents, oxidation state of the metal, or number of unpaired electrons present. Fe_2O_3 shows a higher T_1 contrast effect due to the greater number of unpaired electrons, that is, five unpaired electrons in Fe^{3+} as compared to Fe^{2+} ions-4 unpaired electrons. Fe_2O_3 has 20 percent less magnetization than Fe_3O_4; however, their r_1 relaxivity is the same at the same size.[92–94]

2.3.1.3. *Composition.* Composition is another important parameter that can disturb the T_1 contrast effect. Various contrast agents were incorporated together to gain synergism to enhance the overall T_1 effect. For instance, when Gd^{3+} is incorporated in iron oxide nanoparticles, it disturbs the magnetic spin, lowers the net magnetization value, and increases the r_2/r_1 ratio.[95,96] Thus, the r_1 value decreases and the T_1 contrast effect rises well. Additionally, varying compositions of contrast agents are required for multimodal imaging and real-time monitoring of drug release at the target site. Similarly, pH-responsive contrast agents are of wide concern.[97,98] At neutral pH, agglomeration of the pH-responsive agents occurs, decreasing r_1 relaxivity as well as the contrast effect. Under acidic pH, agglomeration is prevented, and r_1 relaxivity is effectively increased. In this way, early diagnosis of tumors is possible with the help of positive T_1 contrast agents.[66,99]

2.3.2 **T_2 contrast agent.** T_2 contrast agents are also known as negative contrast agents because they increase the rate of decay of transverse magnetization and result in dark image signals. IONPs act both as T_1 and T_2 contrast agents, except they possess greater saturation magnetization, which has a greater influence on T_2 than T_1 relaxation.[100] For iron oxide-based contrast agents, the r_2/r_1 ratio is greater than 1, which means a greater value for r_2 relaxation; hence, they are used as T_2 contrast agents in MR.[101] Notably, the r_2 relaxation time can be significantly increased by improving the saturation magnetization of the contrast agents.

Contrary to T_1 contrast agents, the efficiency of T_2 contrast agents is less affected by higher magnetic fields.[102] Therefore, T_2 contrast agents are preferred for MRI studies at high magnetic fields and preclinical and clinical research. SPIONs are the most widely used T_2 contrast agents owing to their large magnetic moments, which impede T_2 effects. Structurally, SPIONs are composed of a magnetic iron oxide core surrounded by coating material, such as dextran, polyethylene glycol, or silica. The coating offers biocompatibility and stability and allows functionalization for specific targeting or imaging purposes.[103] SPIONs are used in cell labeling experiments as contrast agents for tumor imaging, inflammation detection, and cardiovascular disease diagnosis.[104] However, SPIONs have some limitations, such as potential toxicity, difficulty in controlling their size and magnetic properties, and interference with other MRI techniques.[76,105,106] In addition to stabilizing the particles, surface modifications can also impart specific properties to iron oxide nanoparticles, for example, targeting capabilities or drug loading capacities. Functional groups on the surface of NPs can be used to conjugate targeting moieties, such as antibodies or peptides, to enable specific binding to cells or tissues of interest. Similarly, drug molecules can be conjugated or encapsulated onto the surface of particles for targeted drug delivery.[107,108]

IONPs have a number of advantages over other contrast agents, including biodegradability, biocompatibility, and ease of elimination from the body through usual iron metabolism pathways.[109] They have a long circulation time in the blood, allowing efficient accumulation in target tissues.[110] They also have high relaxivity, meaning they have a strong effect on the magnetic field and produce a significant contrast signal. Furthermore, their superparamagnetic behavior allows detection at very low concentrations by MRI.[111]

In addition, their small size can lead to rapid clearance from the body, which may limit their effectiveness in certain applications.[112] To address this issue, iron oxide, in some cases, may be complexed with other biocompatible materials such as Dextran, peptides, poly(ethylene glycol) *etc.*; however, this may lengthen the clinical approval process due to additional cost and labor.[113,114]

Ultra-small superparamagnetic iron oxide NPs (USPIONs), also known as very small iron oxide particles (SOPs) or monocrystalline iron oxide NPs (MIONs), have a high surface area-to-volume ratio, making them ideal candidates for molecular imaging, drug delivery, magnetic hyperthermia, and targeting applications.[115] USPIONs are easily cleared from the body and have a low toxicity profile. In contrast, SPIONs are larger and have a higher magnetic moment than USPIONs. MPIOs are used for gastrointestinal imaging and can be orally administered. Cross-lined iron oxides (CLIOs) are cross-linked SPIONs used for targeted molecular imaging and drug delivery applications.[116,117]

Another important factor that can influence the relaxivity of SPIONs is the presence of other molecules or ions in the surrounding environment. For example, it has been shown that the relaxivity of SPIONs can be enhanced in the presence of certain ions, such as copper or zinc, which can bind to the surface of the particles and increase the magnetic field inhomogeneities.[105]

In addition to their potential toxicity, SPIONs can also cause artifacts in MRI images owing to their magnetic susceptibility. This can be particularly problematic in regions of high magnetic field gradients, such as the lungs, bones, and air-tissue interfaces. Artifacts can be minimized by optimizing imaging parameters, using alternative contrast agents, or using image processing techniques to fix the artifact.[118] However, the artifacts induced by IONPs can also be advantageous in MRI applications where they result in the enhancement of the contrast effect while increasing sensitivity and detection.[119,120]

The size of IONPs plays a pivotal role in shaping their pharmacokinetics and biodistribution. NPs measuring less than 5.5 nm are eliminated *via* renal excretion. Conversely, larger SPIONs exceeding 200 nm in size are rapidly engulfed by phagocytic cells and accumulate within the monocyte phagocyte system (MPS), notably in macrophages residing in the liver and spleen.[121] Following intravenous administration, SPIONs swiftly reduced the signal-to-noise ratio in the liver and spleen within minutes. In contrast, USPIONs manage to evade MPS uptake, extending their presence in the bloodstream by approximately 2 h, facilitating their targeted accumulation in specific tissues. Over several days, both SPIONs and USPIONs undergo metabolic processes, converting them into soluble, non-superparamagnetic iron.[122,123]

In the realm of medical imaging, SPIONs are commonly used as negative contrast agents in liver imaging. In contrast, USPIONs are typically employed for imaging lymph nodes and as blood-pool agents owing to their distribution within the intravascular extracellular space.[76] They have also demonstrated utility as contrast agents in various applications, including lymphography, angiography, bone marrow imaging, and perfusion imaging of organs such as the brain and kidneys. To achieve optimal contrast-to-noise ratios at standard field strengths and low concentrations of biochemical epitopes, surface modifications of SPIONs can be achieved using active targeting strategies. Various ligands, including polyethyleneimine (PEI), hyaluronic acid, antibodies, small peptides, lectins, aptamers, engineered proteins, and protein fragments, can be introduced into SPIONs to enhance their targeting capabilities for specific tissues or cells. For instance, USPIONs stabilized by 4-methylcatechol coupled with a cyclic arginine–glycine–aspartic acid (cRGD) peptide have been assessed for their potential in tumor-specific MRI targeting.[122,124]

In addition to optimizing the magnetic core, surface modifications of IONPs can also enhance MRI contrast properties. Surface coating with biocompatible polymers can improve the stability, circulation time, and biocompatibility of NPs. Polyethylene glycol (PEG) is commonly used to reduce particle aggregation and prevent recognition by the reticuloendothelial system (RES), thereby increasing circulation time in the bloodstream.[125] PEGylation also reduces nonspecific binding to cells and improves the biocompatibility of nanoparticles. Other surface coatings, including dextran, chitosan, and hyaluronic acid, are employed, which provide additional targeting functionalities. Moreover, the conjugation of contrast agents to target moieties, such as antibodies or peptides, can improve the specificity of the MRI contrast agent to its intended target.[126] However, it is important to note that PEGylation can alter the pharmacokinetics and biodistribution of the particles, which may impact their efficacy as contrast agents.[127,128]

SPIONs were initially developed as T_2 contrast agents owing to their larger size and magnetic moments. A new generation of smaller-diameter USPIONs has demonstrated excellent T_1-enhancing properties. SPIONs produce negative contrasts at the target site, resulting in a blooming effect. However, imaging immediately following SPION administration presents challenges, as their presence in the circulatory system continues to affect T_2^* signals. Consequently, clinicians must wait 24–72 h post-administration to obtain clear MRI images. This phenomenon is well-documented in numerous studies involving imaging of organs within the reticuloendothelial system, such as the spleen and liver. Upon intravenous administration, these NPs are sequestered by the reticuloendothelial system, thereby rendering the contrast agents organ specific. The elevated concentration of these NPs in these organs results in an immediate reduction of the T_2 contrast effect. Thapa *et al.* reported PEGylated SPIONs as T_2 contrast agents, exhibiting a high relaxivity of 123 ± 6 mM^{-1} s^{-1}.[129] The substantial spin–spin relaxivity value indicates that at high concentrations, these NPs significantly diminish T_2 signals. These findings are consistent with the study conducted by Canese *et al.*[130] However, the potential toxicity and long-term side effects must be considered, as discussed by Yang *et al.*[131]

Specific off-resonance pulse sequences and ON-resonant water suppression inversion recovery MRI techniques have been proposed to address these limitations, although they do not eliminate signal loss or magnetic susceptibility artifacts.[132] Alternative approaches under exploration involve Microparticles of Iron Oxide (MPIO) and Colloidal Iron-Oxide Nano-Platforms (CIONPs) to enhance the detection of biosignatures at very low nanomolar densities; Table 1 lists the values of R_1 relaxation, R_2 relaxation, size, and saturation magnetization of IONPs with different coatings. From Table 1, it is also concluded that there is a significant lack of comprehensive literature providing these values.

Superparamagnetic iron-oxide nanoparticles (SPIONPs) are composed of iron oxide crystals coated with a biocompatible material to prevent aggregation and provide stability under physiological conditions.[106] SPIONPs are T_2 contrast agents, which means that they shorten the T_2 relaxation time of the surrounding water protons, leading to a decrease in the signal intensity in T_2-weighted images. The advantage of SPIONPs over paramagnetic chelates is their higher magnetic moment, which makes them more efficient under higher magnetic fields. Furthermore, their signal intensity does not decrease at higher field strengths.[76,152]

SPIONPs have been extensively used for cell labeling and tracking studies, as they are engulfed by cells through endocytosis and remain there for a longer period. For example, SPIONs have been applied in liver imaging and tumor targeting owing to their preferential accumulation in these tissues and the enhanced permeability and retention (EPR) effect. SPIONPs have a good safety profile and are well-tolerated by the body; however, their clinical use is hampered by their low sensitivity and specificity-nonspecific distribution in the body.[153] To improve diagnostic and therapeutic applications, ongoing research has focused on developing targeted SPIONPs that can selectively bind to specific cell types or tissues.

Zhao *et al.* pointed out that early-stage tumor metastases may be nonvascularized and incapable of exhibiting the EPR effect.[87,154] The BBB and BBTB present formidable obstacles that hinder the effective delivery of therapeutic agents, including metallic nanoparticles, to the tumor site.[155] The densely fibrotic tumor microenvironment of glioblastoma further impedes nanomedicine delivery, making the EPR effect insufficient to achieve a significant therapeutic effect.[156] Interestingly, some studies have shown that BBB permeability can be temporarily increased under certain conditions, allowing for enhanced nanoparticle accumulation. For instance, Boyd *et al.* demonstrated that the opening of tight junctions in the BBB following traumatic brain injury allows for the accumulation of large drug carriers, such as stealth liposomes, in a manner like the EPR effect seen in other tumor types. However, this window of opportunity is limited, with the barrier closing between 8 and 24 h after injury.[157] To overcome these limitations, researchers have explored various strategies to enhance nanoparticle delivery to glioblastomas. These include the development of BBB-regulating nanovesicles, use of ultrasmall NPs that can cross the BBB,[155] and exploitation of active transport mechanisms.[158] Additionally, novel approaches, such as bacteria-based drug delivery strategies are being investigated to bypass BBB/BBTB and achieve targeted delivery to glioblastomas.[159]

The performance of T_2 contrast agents also depends on the following factors.

2.3.2.1. *Size of contrast agent.* T_2 contrast effect is directly proportional to the saturation magnetization of the IONPs acting as T_2 contrast agents. The saturation magnetization increases with an increase in the size of the IONPs; therefore, larger IONPs exhibit a higher r_2 relaxivity rate.[160] When the IONPs enter a certain size regime called the static dephasing regime, maximum magnetization is attained by the agents, and their diffusion now has little effect on the T_2 relaxation rate. IONPs in this size regime behave as ferrimagnetic; therefore, they retain certain remanent magnetization that is responsible for their agglomeration in the biosystem, which can cause problems during their bioassays. When the size of IONPs enters the echo-limiting regime, the r_2 relaxation rate decreases as not many spins are focused by the echo sequence because larger NPs undergo quick dephasing.[161,162]

2.3.2.2. *Composition of contrast agent.* In spinel ferrites, the distribution of cations in the octahedral and tetrahedral sites determines their magnetic properties. As discussed, earlier T_2 relaxation rates depend on the saturation magnetization of the IONPs; therefore, cationic distribution in spinel ferrites play an important role in enhancing the T_2 contrast effect during MR imaging. For Fe_3O_4 the number of Fe^{3+} at octahedral and

Table 1 Values of R_1 relaxation, R_2 relaxation, size, and saturation magnetization of ferrites with different coatings

Magnetic nanostructure	Size (nm)	Saturation magnetization (emu g^{-1})	R_1 relaxation $mM^{-1}\ s^{-1}$	R_2 relaxation $mM^{-1}\ s^{-1}$	Method	Ref.
PPy/Fe_3O_4/SiO_2/Au	65	3.6	11.85	119.35	Microemulsion	133
Fe_3O_4-MTX@HBc NPs	11.7	9.1	—	—	—	134
SiO_2/Fe_3O_4–Au	280	—	—	—	Sol–gel	135
GdIO nanocomposites	13.1	33.5	70.10	173.55	—	136
Mn–Zn ferrite/SiO_2	7	3.72	—	—	Thermal decomposition	137
GO-coated Fe_3O_4 nanocomposite	50	60.2	—	—	Solvothermal	138
α-Fe_2O_3/Au	49.3	—	—	—	Hydrothermal method	139
LDM-PLGA magnetic nanoparticles	336	—	—	—	Emulsion	140
Fe_3O_4@Ru	100	50.09	—	120.81	Solvothermal approach	141
$NiFe_2O_4$/C	38.2	6.17		78.9	—	142
Fe_3O_4@C@PMOF		24.5	1.23	59.91	Solvothermal	143
WS_2-IO/S@MO-PEG	182	—	—	—	—	144
MnO_2@BSA	20–30	__	18.76	—	Biomineralization	145
DOX/IONPs-FA	50	68.2	—	247.3	Hydrothermal method	146
Gd_2O_3@BSA	20–30	—	10.45	—	Biomineralization	145
Bi_2S_3-GdNanoparticles	170	—	11.9	—	Multi step synthesis	147
MnO_2@Tf-ppIX	30	—	11.07	—	Biomineralization	148
PEGylated PPys@Fe-PDA	__	—	5.055	—	—	149
PPy@Fe_3O_4/Au	—	—		128.57	—	138
DOX/OA-Fe_3O_4@CS-PEG	80	4.11	—	—	—	150
Fe_3O_4-Dox	40	53.15	—	—	—	151

tetrahedral are equal; therefore, they cancel out the effect of each other, and hence, no net magnetization due to Fe^{3+} ions is observed. However, Fe^{2+} ions present at octahedral sites cause some magnetization. Thus, doping with other divalent ions, such as Mn^{2+}, Ni^{2+}, and Co^{2+}, can significantly control the magnetic properties of IONPs. When Mn^{2+} is doped in place of Fe^{2+}, the saturation magnetization increases owing to the presence of five unpaired electrons in Mn^{2+}. So r_2 relaxivity of Fe_3O_4 *i.e.*, 218 $mM^{-1}\ s^{-1}$ increases to 358 $mM^{-1}\ s^{-1}$ after doping with Mn^{2+}.[163–165] SIONPs have also been extensively explored owing to their potential application in multifunctional therapy. Various nanocomposite-based theranostic agents have recently been used to diagnose and treat the affected site, as explained in the subsequent section.

SIONPs are the most used T_2 contrast agents for MRI owing to their inherent properties of producing an enhanced contrast effect that enables noninvasive diagnosis of cancer cells. Moreover, they provide improved SAR values helpful in hyperthermia to kill cancer cells. In this approach, $Mn_{0.6}Zn_{0.4}Fe_2O_4$ NPs have been investigated as MRI contrast agents for *in vivo* imaging of brain activity and the tumor microenvironment.[166,167] Wang *et al.* have synthesized $Mn_{0.6}Zn_{0.4}Fe_2O_4$ and coated them with mesoporous silica NPs (MMSN-RBITC) to fabricate a self-healing hydrogel system composed of natural biopolymers pullulan (PULL) and chitosan (CS). The system was then loaded with anticancer drugs, such as DOX, rhodamine B isothiocyanate, and mesoporous silica-coated $Mn_{0.6}Zn_{0.4}Fe_2O_4$ nanospheres. This composite system is used as an MRI contrast agent in addition to a therapeutic agent to treat cancer cells. These nanocomposites were also applicable efficiently in magnetothermal chemo-dynamic cancer therapy owing to the synergistic effect. These IONPs, when loaded with DOX, offer self-healing properties and have proven to be efficient materials for both MRI and drug delivery.[137]

α-Fe_2O_3 NPs coated with gold NPs provide biocompatible nanostructure that has multifunctional diagnostic and therapeutic functions. They have been successfully used to prevent and reduce the growth of 4T_1 tumor cells during radiotherapy and photothermal therapy. PPy/Fe_3O_4-core gold nanostructures have been reported for multimodal imaging, including optical and MR imaging. Gold nanostructures are theranostic agents that are responsible for the strong absorption of near-infrared radiation. Polypyrole is a good therapeutic and photothermal agent that provides better compatibility with biosystems along with thermal stability. The prepared magnetic nanostructure retained properties that suit it as a contrast agent for both MRI and X-ray computed tomography, thus acting as a multimodal scanning contrast agents.[133]

Modern research is focused on theranostic agents because of their ability to simultaneously diagnose and treat problems. In another investigation, gold, iron oxide, and porous silica were combined into a single agent, followed by incorporation of anticancer drugs such as DOX and Ce6 into the pores of silica [M-MSN(Dox/Ce6)]. This combination is not only helpful in MR and CT scanning but also in delivering anticancer drugs to the affected area. Moreover, the drug resistance problem is also a struggle to uphold the required amount of drug dose inside the system. To deal with drug resistance, p-glycoprotein (P-gp) small hairpin RNA (P-gp shRNA) was introduced in the composite, that is, M-MSN(Dox/Ce6)/PEM/P-gp shRNA.

Magnetic silica has been extensively investigated in this context; for example, magnetic nanoporous silica decorated by photosensitizer chlorin and DOX was explored for MR efficiency and magnetic drug delivery.[135]

Albumin based nanocomposites of Gd_2O_3@BSA and MnO_2@BSA were also investigated and used for MR imaging of myocardial infarction in model rabbits, where MnO_2 is a pH-responsive motif and Gd_2O_3 is a non-pH-responsive motif, both acting as T_1-weighted positive contrast agents. The protein provides a basis for the growth of nanostructures and biocompatibility of the composite system. At a low pH of 6.5, the pH-responsive MnO_2 releases Mn^{2+}, which interacts with the protein molecules, increases relaxivity, and enhances MR imaging.[145] MnO_2@transferrin (Tf) is used for MR imaging of glioblastoma, where transferrin is an important glycoprotein that can combine with transferrin receptors and transverse the blood–brain barrier. Protoporphyrin is then conjugated with MnO_2@transferrin and acts as a photosensitizer. After entering the tumor site, the system responds to the low pH of the microsystem and releases Mn^{2+} ions and oxygen, thus enhancing MR imaging.[148]

Other pH-responsive systems used in MR imaging have also been investigated, including metal dichalcogenides, such as MoS_2, WS_2, Bi_2Se_3, and TiS_2 sheets. A multi-functional system of WS_2, consisting of IONPs coated with silica, which is then sequentially obscured by MnO_2 and polyethylene glycol (WS_2-IO/S@MO-PEG), is studied for multi-modal MR imaging. This consists of T_2 weighted SMIO contrast agent plus T_1 weighted MnO_2 pH-responsive contrast agent to enhance MR imaging, and PEG to increase biocompatibility for radio therapy and photothermal therapy.[167]

3. Drug delivery

Drug delivery is an important aspect of biomedical research. Magnetic NPs have shown dramatic results in this field owing to their biocompatibility, non-immunogenicity, and minimal hazardous effects. Drugs attached to magnetic NPs can move directly towards the target site with the help of an external magnetic field. There are various factors that affect their efficiency, including the uncontrollable release of the drug before the NPs reach the target site and issues related to drug loading.[168,169] Such problems can be mitigated by specific coating agents, which not only enhance biocompatibility but also help the drug to be released at the target site (Fig. 6).[170,171]

As mentioned previously, magnetic NPs are mainly composed of iron oxide, with the most common forms being magnetite (Fe_3O_2), maghemite (γ-Fe_2O_4), and hematite (α-Fe_2O_4). Other elements are often involved, for example, ferrites of cobalt, chromium, nickel, and boron. Because of the possibility of different forms of iron oxide, it is important to monitor the experimental parameters to ensure that a single phase of iron oxide is used.[172]

Only superparamagnetic NPs are useful for drug delivery. Their lack of magnetization after the removal of the external magnetic field helps resolve the serious problem of particle agglomeration.[173] Under these conditions, the NPs do not agglomerate and maintain their size dimensions comparable to those of viruses and proteins, that is, 20–500 and 5–50 nm, respectively. Targeted drug delivery by magnetic NPs has a significant advantage over other delivery systems in that it reduces drug wastage and leads to reduced drug administration frequency. The efficiency of drug delivery depends on various

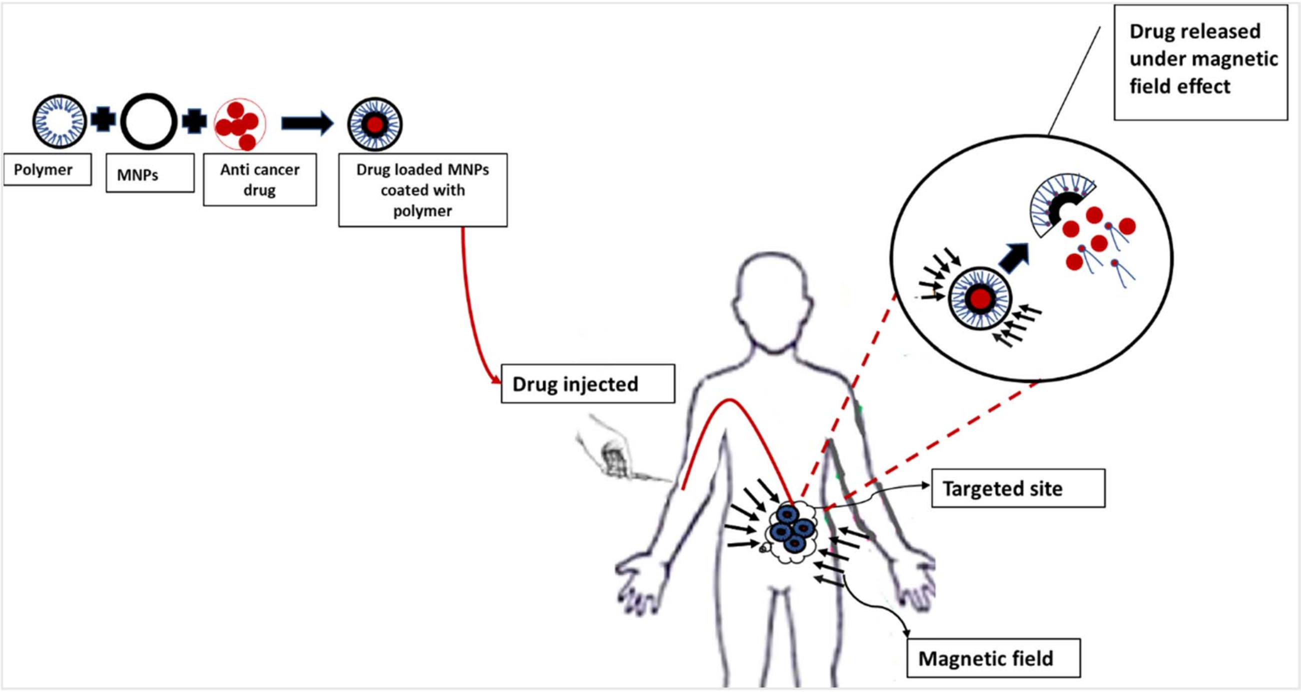

Fig. 6 Principle of magnetic drug delivery.

factors such as magnetic field strength, size of magnetic NPs, magnetization of magnetic NPs, blood flow rate, and vascular supply.[174,175]

3.1 Toxicity of magnetic nanoparticles

The toxicity of magnetic NPs has been extensively studied both *in vivo* and *in vitro*. In general, their cytotoxicity was very low. Initially, magnetic NPs containing iron were considered non-toxic because of the physiological presence of iron inside the cell cytoplasm in the form of special proteins called ferritins.[176] It was postulated that ferric ions released after the breakdown of magnetic NPs would be metabolized in the same way as cytoplasmic iron. However, because of the nano-size of the particles, there was a greater concentration of iron in the system, which could lead to the formation of free radicals. Currently, the dose of NPs administered during drug delivery should not exceed the threshold level of 100 μg mL^{-1}.[177] Any amount exceeding this limit is considered toxic. Finally, because of their small size, magnetic NPs have a large surface area and offer more sites for the adsorption of different ions and protein molecules present in the cell medium.[178]

3.2 Functionalization of MNP's for drug delivery

Coating magnetic NPs with polymers, amino groups, silica, and various surfactants enhances their biocompatibility and helps in attaining better dispersion and preventing agglomeration during drug delivery. These coatings also provided better stability against oxidation and enabled the particles to transport high drug dosages in the coating shell.[179]

3.2.1 Polymer coating. During *vivo* applications, leaching of the drug and other components of the NPs that are toxic to the system is a serious issue. Polymer coatings provide shells around the particles, thus preventing them from leaching into the system. Most naturally occurring polymers are suitable for coating purposes because of their high biocompatibility, for example, carbohydrates and proteins. Carbohydrates such as dextran have been extensively used either singly or in combination with other polymers. Magnetic NPs coated with dextran are now available commercially.[180,181]

Natural polymers suffer from the drawbacks of high water solubility and low mechanical strength. These problems can be overcome using synthetic polymers, which have cross-linkages between the layers and thus have better mechanical strength. Some examples of synthetic polymers include polyethylene glycol, poly L-lactic acid, and polyvinyl alcohol. The presence of pores in the polymer shell is also a problem for synthetic polymers because these pores can facilitate the oxidation of the magnetic core.[182,183]

3.2.2 Protein coating. Protein coatings on NPs have also been widely investigated for biomedical applications. NPs functionalized by some natural proteins are now known, such as albumin and lipids.[183]

3.2.3 Silane coating. Some organosilanes are also helpful in providing surface modifications suitable for protein conjugation.[184]

3.2.4 SiO_2 coating. Because of its high mechanical strength, amorphous silica is also used for coating purposes.[185]

Multicomponent NPs provide a synergistic approach to the inhibitory mechanism as the individual components contribute together, thus enhancing overall efficiency. When magnetic iron oxides are combined with polymers, this combination provides organic and inorganic contributions.[186] Magnetic NPs exhibit the outstanding property of being readily detectable and guided by magnetic fields, but their lack of biocompatibility has always remained a problem.[187] Magnetic nanocarriers have low dispersibility; therefore, they must be modified to overcome such problems. Polymers, on the other hand, are biocompatible and biodegradable; hence, when combined, they play a stronger role than individually.[188] In this regard, one-pot synthesis has been used to synthesize niclosamide-encapsulated, hyaluronic acid-functionalized core–shell nanocarriers [(NIC-PLGA NP) HA]. Niclosamide is used as a drug to inhibit cancer cell growth. When it was encapsulated in nanoparticles, the loading efficiency was approximately 7.1%. These NPs showed high cytocompatibility upon testing with MDA-MB-231 and L929 cell lines; the cancer cell inhibition rate was approximately 85%, a highly convincing result.[189] Hollow magnetic nanospheres were also prepared and combined with chitosan and acrylic acid. A phantom MRI test showed that these spheres had an important MR signal improvement in a T2-weighted image.[189]

3.3 Applications for nanoparticulate delivery systems

For the application of magnetic NPs in biomedicine, surface modification is performed to overcome certain problems. Without any functionalization, there would not be a strong interaction between the NPs and biomolecules, and this may cause the early release of the NPs into the system. After surface modification, there is a strong interaction, and the particles are prevented from agglomeration. Commercial organic linkers, such as thiols, amines, aldehydes, and carboxylic acids, are also helpful in the surface modification of IONPs.[190]

Opsonization refers to the binding of protein molecules to the surface sites of NPs.[191] This phenomenon facilitates rapid elimination through phagocytosis by phagocytic cells, aiding rapid protein clearance from the body. Factors influencing NPs(NPs) clearance and biodistribution include[192] nanoparticle sizes that play crucial roles in regulating NPs' circulation and biodistribution through hepatic filtration, tissue extravasation, and kidney excretion during their journey in the body. NPs <10 nm in size are rapidly cleared *via* the kidneys or extravasated. In addition, NPs' uptake by MPS cells is affected by surface charge. Positively charged NPs evoke higher immune responses than neutral/negatively charged NPs. Neutrally charged particles exhibit lower opsonization rates than charged ones.[192] Moreover, PEGylation involves modifying NPs surfaces with PEG, offering favorable physicochemical properties that mitigate NPs accumulation in target organs. Ligand functionalization can also involve attaching target ligands to the PEGylated NPs surfaces.

3.4 Targeted drug delivery

Efficient drug delivery can be achieved through the utilization of targeting ligands on NPs surfaces. These surfaces are commonly altered with organic polymers and inorganic metals or oxides to enhance biocompatibility and enable subsequent functionalization by attaching diverse bioactive molecules.[193] The approach to localizing drugs using magnetic delivery systems relies on the interplay between forces from blood components and magnetic forces stemming from an external magnet, as particles compete within this dynamic framework.

Fig. 7a depicts the process of targeted drug delivery using magnetic NPs to tumor cells *via* receptor-mediated endocytosis. In this mechanism, drug-loaded IONPs navigate through the bloodstream to designated tumor cells. Upon interaction, they enter the cells by forming an endosome. Subsequently, the endosome expands owing to heightened osmotic pressure, ultimately rupturing to discharge the drug within the tumor cells. Fig. 7b presents the *in vivo* magnetic resonance images of a mouse following the administration of drug-loaded NPs at varying time intervals.

3.4.1 Factors responsible for effective drug delivery. The level of accumulation of IONPs plays a crucial role in their targeting efficiency. In 2016, Wilhelm *et al.*[195] studied dosage efficiency and found that medium doses of drug-loaded NPs *via* a passive route caused 0.6% accumulation in tumors. When the route was changed from passive to active, the accumulation improved, but only to 0.9%. Hydrostatic pressure plays an important role in the accumulation process. Tumor tissues have greater hydrostatic pressure than normal cells/tissues, which leads to a greater accumulation of NPs at the tumor site. These researchers also found that the efficiency of drug delivery depends on the microenvironment of tumor tissues. Tumors with different tissue structures complicate the system for drug delivery. Once NPs are injected into blood vessels, they are carried to the target sites.

3.4.2 Magnetic drug targeting. Magnetophoresis is a mechanism that involves a magnetic field and magnetic nanocarriers to carry loaded drugs to the targeted sites of tumors.[196] In this method, the drug is loaded in a magnetic nanoparticle and encapsulated by a capping agent to ensure biocompatibility. Finally, these magnetic nanocarriers are injected into the body *via* blood vessels and steered to the site of interest with the aid of an external magnetic field. The magnetic field helps accumulate the drug at the tumor site without it being released at other healthy sites. Therefore, this process not only prevents wastage and undesired drug release but also aids in reducing the risk of any side effects. Several studies have been conducted on animals, such as mice and rabbits, where magnetic nanocarriers were used under an external magnetic field for drug accumulation.[197] In humans, magnetic drug

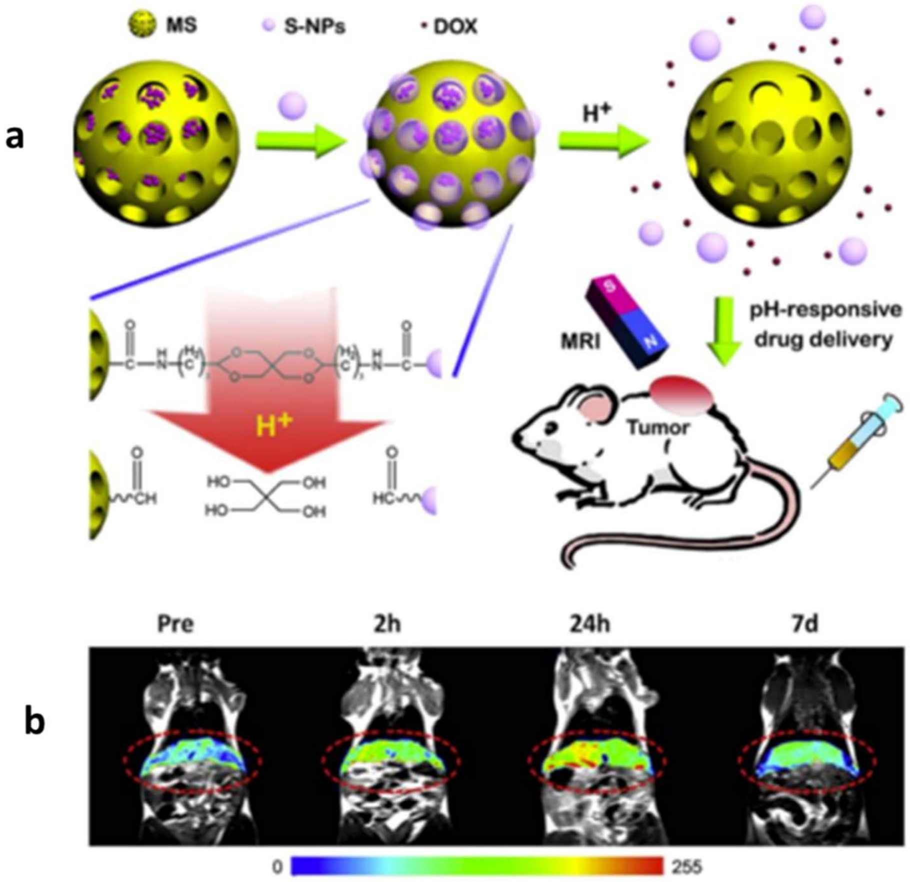

Fig. 7 pH responsive drug delivery of DOX based drug (a) and MR images at different intervals (b). Copyright 2015, Elsevier.[194]

delivery was first attempted in 1996 to accumulate epirubicin in sarcomas.

Another problem associated with drug delivery and accumulation is the distance of the target site from the blood vessels where the drugs are injected into the body. Lübbe *et al.* 2001[198] performed clinical trials of drugs loaded in magnetic nanocarriers and detected that tumors only 5 mm below the body surface were susceptible to drug delivery. Another attempt by Rotariu and Strachan (2005) showed that rare-earth magnet targets 18 mm from the body surface could be activated using NPs smaller than 500 nm. Increasing the size of the NPs up to 5 μm and targeting at a distance of 15 cm is achievable, but there are problems with the circulation time in the bloodstream.[199]

To improve magnetic targeting for deep targets, it is necessary to design NPs that can penetrate the surface and can sustain an effective circulation time. SPIONs have been shown to be particularly effective in this respect. SPIONs coated with polymers, such as polylactic acid-*co*-glycolic acid–polyethylene glycol, were subjected to numerous tests by Al-Jamal *et al.* (2016).[200] They found that nanoparticle accumulation initially increased with higher SPION concentration, but eventually after a certain concentration was reached, no further improvement was noted.

3.4.3 Improving magnetic targeting with steering coils and multi-magnet systems. The effective field gradient from the external magnetic field is also an important factor in magnetic targeting. The field gradient must be sufficiently strong to penetrate greater depths inside the patient. Steering coils and multimagnet systems are effective in this regard. A catheter was used to pass the drug-loaded magnetic nanocarriers into the blood vessels as close as possible to the tumor site.[201] After injection of the nanoparticles, steering coils were used to focus the particles on the target site. However, this method still requires larger sized NPs of about 50 μm and in some cases 1.5 mm in diameter. Owing to their large size, these particles cannot pass through the pulmonary veins and can only be introduced through the arterial system.[202,203]

Multi-magnet systems have also been employed to improve the targeting efficiencies of magnetic NPs. These systems include Halbach arrays, which increase the magnitude of the targeting field. Different forms of Halbach arrays have been used, including linear and cylindrical arrays. To further improve the targeting field gradient, some researchers have used susceptible materials, such as steel, which allows the magnetic field to pass through it. Such materials can produce higher field gradients; therefore, the field can be focused on certain regions and guide the magnetic carriers to accumulate at the target site. Electromagnetic coils are also a good alternative to permanent magnets.

All the methods described above tend to produce strong field gradients. However, there is also a problem associated with them. The magnetic NPs accumulate at the site near the magnetic device and do not penetrate the tumor site. An alternative approach to solve this problem has been developed by Krzyminiewski *et al.*, in which two oppositely charged magnets are used that can be rotated about an axis to concentrate the magnetic nanocarriers at the center, thus keeping them away from the device.[204,205]

3.5 Mechanism of drug release

After reaching the target site and accumulating in the tumor, these magnetic NPs can perform various functions. Under the influence of an alternating magnetic field, the particles tend to align their magnetic moments along the field and release thermal energy into the surroundings. Because of the change in the alternating field, the amount of heat dissipated increases, and it can be used in hyperthermia to kill cancerous cells, which are temperature sensitive. Moreover, this dissipated heat can also help in magnetic-induced drug release for thermally sensitive NPs.[168,206–208] Table 2 lists the values of size, zeta potential, and saturation magnetization of different magnetic loaded with the drug NPs. In a study by Hu *et al.*,[211] the anticancer drug tamoxifen was delivered to the target site by loading it with magnetite NPs coated with L-lactic acid. The particles were synthesized using a solvent evaporation/extraction technique in an oil–water emulsion. The drug-loaded NPs were then tested against breast MCF-7 cancer cells. NPs with sizes of approximately 6 nm coated with L-lactic acid caused a saturation magnetization of 7 emu g^{-1}. The tamoxifen-loaded magnetite/poly(L-lactic acid) particles (TMCN) were then examined for their cytotoxicity and uptake by cancerous cells. Approximately 80% of the cells were killed after a 4 days incubation period. These results show that TMCN NPs are useful as carriers for the targeted release of tamoxifen.[211] Targeted drug delivery involves many factors that must be considered when transmitting a drug to a target site. Some components of the delivery system are temperature-sensitive and only release the drug at a certain temperature. Similarly, many magnetic NPs guided by an external magnetic field are affected by temperature and/or pH changes. Das *et al.*,[209] have achieved a one-pot synthesis of urethan-linked magnetite NPs coated with β-cyclodextrin that are able to transport both hydrophobic and hydrophilic drugs. When loaded into these nanoparticles, the DOX drug is temperature sensitive and drug release occurs at an elevated temperature, but the pH conditions also affect the release of the drug. Drug release follows diffusion, and because of the fluorescent nature of the nanoparticles, it is relatively easy to track their path. *In vitro* studies have also confirmed their biocompatibility and nontoxicity to healthy cells with a remarkable efficiency of killing cancer cells at low concentrations.[223] Nanoconjugates have been observed to increase endocytosis of the bioavailable drug curcumin. Subsequent *vivo* work together with *in vitro* data have revealed a substantial tumor reversion when drug-loaded nanoconjugates are employed.[167,209]

Magnetization also plays an important role in improving the efficiency of IONPs for targeted drug delivery. The problem of biocompatibility and biodegradability is also an important issue to address. To develop a delivery system encompassing both of these parameters, a composite of magnetite and poly(D,L lactide-*co*-glycolide) (PLGA) was prepared using an oil/water emulsion and solvent evaporation technique.[210] A magnetite

Table 2 Size, zeta potential, and saturation magnetization of different IONPs with loaded drug

Nanoparticles	Loaded drug	Size (nm)	Zeta potential (mV)	Saturation magnetization (emu g^{-1})	Applications	References
β-Cyclodextrin based nano conjugates	Curcumin	55–65	—	97.65 emu	Anti-cancer activity	209
Magnetic poly (D,L-lactide-*co*-glycolide) nanospheres		360–370	−34 to −36	26–40 emu g^{-1}	Drug delivery	210
Magnetite/poly (L-lactic acid) composite	Tamoxifen	195–209	−13 4 to −21 1	7 emu g^{-1}	Anti-cancer activity	211
Magnetite/poly (alkyl cyanoacrylate)	Tegafur	30	−30 to −35	<10 emu g^{-1}	Anti-cancer activity	212
Fe_3O_4@LEC-CUR-PLGA-MMS	Curcumin	200	—	47.09 emu g^{-1}	Drug delivery	213
BIONPS/EPPT//DOX-HCL or PTX	DOX-HCL PTX	167–188	−5 to −30	10.1–9.6	MRI/fluorescence imaging, and anticancer drug delivery	214
Polymeric poly lactic-*co*-glycolic acid (PLGA)	Nisin	246–445 nm	−3.6 to 16.9	—		215
$ZnFe_2O_4$-hydroxyapatite nanocomposite	3-(4,5-Dimethylthiazol-2-Yl)-2,5-diphenyl-tetrazolium bromide	40–130	—	7 emu g^{-1}		216
(NIC-PLGA NP) HA	Niclosamide	150.8	−24.9	—	Targeted cancer therapy	189
Fe_3O_4/chitoan–poly(acrylic acid) hybrid		200	35.6	40.7 emu g^{-1}	Targeted drug delivery	217
Magnetic gold nanoparticles	Doxorubicin	22	−31.1	—	Targeted drug delivery	218
SPION@HP core–shell	Doxorubicin	17.7	—	24.92 emu g^{-1}	Targeted drug delivery	219
(Poly-*N* isopropyl acrylamide-*co*-poly-glutamic acid)/($MnFe_2O_4$)	Curcumin	37	—	348.0 emu g^{-1}	Targeted drug delivery	220
NIR-830-ZHER2:342-IONP-cisplatin	—	—	—	—		221
Pine pollen-based micromotor (PPBM)	—	—	—	—		222

concentration of 40–60% was found to be sufficient to obtain a good value of saturation magnetization (26–40 emu g^{-1}), while the polymer content was also sufficient to provide reasonable biodegradability to the nanoparticles. Such high magnetization coupled with low oleic acid content provides a better platform for magnetically guided delivery, hyperthermia, and magnetic resonance imaging (MRI) contrast agents.[210] The applicability of magnetic nanocarriers is due to their responsiveness to magnetic fields and compatibility with biosystems. A study was conducted in which a core/shell of polymer around a nucleus of magnetite NPs was prepared *via* an emulsion polymerization method.[212] The polymer helped to prevent agglomeration of the particles and to provide the needed biocompatibility. The NPs were also equipped with the anti-cancer drug Tagafur. Spectrophotometry and electrophoretic studies have shown that there are two mechanisms involved. One mechanism is absorption, and the other is surface adsorption. The presence of the polymeric coating also reduced the magnetization of the magnetite core, but the ferrimagnetic nature remained intact. The type of polymer, pH, and drug concentration are factors that control drug absorption on NPs.[212]

IONPs of Fe_3O_4@LECCUR-PLGA-MMS were synthesized using a green technique where watermelon rind extract was used in a biogenic process without using toxic chemicals for the reduction or oxidation processes. Fe_3O_4@LECCUR-PLGA-MMS NPs were used as an ROS-sensitive drug release system, and these particles were synthesized by a double emulsion method. Subsequent MTT, fluorescence, and colony formation assays also revealed that the Fe_3O_4@LEC-CUR-PLGA-MMS particles can be potential anticancer agents as they were toxic to cancer cells while being cytocompatible with healthy cells. This delivery system is sensitive and responsive to an ROS environment, including H_2O_2, and releases the drug curcumin (CUR) into the environment. Greater cytotoxicity was found for A549 and HeLa S3 cancer cells after 24 h of incubation, and it was also possible to limit the A549 cell colony as compared to healthy cells.[213] Another approach to designing suitable magnetic nanocarriers involves preparing polymeric poly lactic-

co-glycolic acid (PLGA) NPs for conjugation with blood protein spectrin (SPN). A double emulsification solvent evaporation method was then used for the encapsulation of the drug nisin. More than 64% of drug entrapment was observed, with 85% drug release. An *in vitro* cytotoxicity study was achieved by performing a sulforhodamine blue assay on MDA-MB-231 (breast cancer) and FR-2 (normal breast tissues) cells. The IC_{50} values for unconjugated and SPN-conjugated NPs were 13.0 and 0.06 $\mu g\ mL^{-1}$, respectively, on MDA-MB-231 cells, and 276.11 and 142.99 $\mu g\ mL^{-1}$ on FR-2 cells. It does appear that these NPs could indeed be used for improved cancer treatment without any toxic effects on normal cells.[215]

A significant inhibitory effect of $ZnFe_2O_4$–HA NPs on bacterial proliferation and growth was noted for an optimal dose of 0.078 $mg\ L^{-1}$. A co-precipitation technique was employed to synthesize $ZnFe_2O_4$–hydroxyapatite (HAp), $ZnFe_2O_4$, and nanostructures. Moreover, dose-dependent cytocompatibility tests of the NPs on both HEK normal cells and G292 cancerous cells were performed using a 3-(4,5-dimethylthiazol-2-yl)-2,5-diphenyltetrazolium bromide (MTT) assay. All the NPs were cytocompatible and no cytotoxicity effects on normal and cancer cells were observed in the dose-dependent test, and the NPs prevented cancer cell spread and growth.[216]

Nowadays, researchers are focusing on NPs that can perform multifunction, such as targeting drug delivery, hyperthermia, MRI, and other specific functions. A multifunctional nanoparticle system comprising oleic acid-Fe_3O_4 NPs (OA-Fe_3O_4) encapsulating doxorubicin hydrophobic (DOX-HCL) was prepared using the double emulsion solvent evaporation technique. The drug release rate was responsive to pH and decreased with increasing environmental pH. The cytotoxicity of the drug-loaded system was tested *in vitro* against MCF12-A and MCF-7 breast cancer cells. Additionally, an *in vivo* procedure was performed in BABL/c mice. There was a significant decrease in cell viability for the BIONPs/EPPT system compared with other nanoparticles. Furthermore, the drug-loaded BIONPs/EPPT NPs produced a significant decrease in tumor volumes compared to other NPs.[214]

In another study, the polymer heparin was incorporated into SIOMNPs. The anticancer drug doxorubicin (DOX) was then loaded in the system with a loading efficiency of 66.9%, and the drug was released in a controlled manner within a time interval of 120 h without any burst release. Owing to sufficient loading, the SPION/heparin NPs loaded with doxorubicin exhibited improved anti-cancer effects against HeLa cells.[219] Similarly, in another attempt, magnetic gold NPs were first synthesized and decorated with thiol-terminated polyethylene glycol (PEG) and then loaded with doxorubicin. This formulation also helps to minimize the random distribution of the drug and prevents healthy cells from being affected by the drug through targeted delivery.[218] Poly N isopropyl acrylamide-*co*-poly glutamic acid was also tested in combination with superparamagnetic iron oxide nanoparticles. The loading efficiency was 89% with fast drug release at a pH of 5.5. These NPs were loaded with curcumin and tested for drug delivery efficiencies; the response was very fast, and 99% of the magnetic NPs were collected near the magnetic field source within 2 min. Moreover, these particles exhibited antibacterial properties against *E. coli*.[220]

Tumor heterogeneity and resistance to anticancer drugs limit the efficiency of therapy.[224] To address this issue, Satpathy *et al.* developed an efficient system for the treatment of ovarian cancer cells. They proposed a system composed of iron oxide magnetic NPs coated with amphillic polymer and labeled with a dye (HER2) and the anti-cancer drug cisplatin. This conjugate system carrying the drug was found to significantly inhibit the growth of ovarian cancer cells in mice (xenograft model). Similarly, the conjugate system had a long retention time that allowed the response of drug-resistant tumor cells and the conjugate system.[221] Currently, research is in progress on the use of micromotors in the field of efficient drug delivery systems due to their promising ability for *in vivo* drug delivery. However, developing such a system with controllable drug release, suitable biocompatibility, and flexibility remains a challenge. In this approach, pine pollen-based micromotors (PPBM) have shown significant results for targeted drug delivery. With the help of vacuum loading, the two air sacs of pine pollen were encapsulated with iron oxide NPs and the anti-cancer drug. This remains an economical and massive fabrication technique. Moreover, along with controllable drug release, the micromotor-based system displayed a drug release based on demand that could be controlled by the agglomeration of iron oxide NPs under a high magnetic field. Thus, the magnetic field can be used for transporting the drug along with controllable and desirable drug release.[222]

4. Hyperthermia

Traditional methods of cancer treatment include chemotherapy and oral medications. The latter approach has several undesirable side effects, including dosage levels that must not be exceeded to avoid damaging normal cells.[225] Similarly, chemotherapy also has many side effects, such as the destruction of healthy cells due to non-targeted therapy on cancer cells. With the development of nanotechnology, the field of nanomedicine has benefitted from the introduction of a wide variety of nanomedicines, nanotherapeutics, and diagnostics for the treatment of cancer cells. Hyperthermia is used in combination with radiotherapy to avoid damage to the healthy cells that normally happen in radiotherapy alone. Hyperthermia can act as a sensitizer for specific cancerous cells prior to radiotherapy, thereby increasing problems of biotoxicity and hemocompatibility ng the efficiency of the method. Hyperthermia can also reduce the harmful effects of radiotherapy on the surrounding tissues.[226]

Active tumor targeting can be achieved by either manipulating external factors or modifying the nanoparticles themselves. Different approaches have been employed for active tumor targeting including intratumoral administration, external stimuli, and transcytosis through vascular endothelial cells.[227] Urbano-Gámez *et al.*, comprehensively discussed all these approaches for targeting tumor *versus* tumor cells in a review.[228]

Hyperthermia is a modern therapeutic modality utilized for the eradication of malignant cells through the targeted delivery of IONPs to the affected site, followed by their subsequent heating *via* an externally applied magnetic field.[229] Magnetic NPs offer the advantage of precise targeting specific sites without causing harm to nearby cells when subjected to an external magnetic field to heat cancer cells. This combines therapeutics with diagnosis, along with monitoring of the material at the cancer site.[230] This heating effect arises from Néel and Brownian relaxations, wherein the magnetic NPs generate heat owing to the friction caused by their oscillations when exposed to a magnetic field. The temperature of the cells is maintained at 41–47 °C, the range in which abnormal cells are more susceptible to destruction due to their elevated metabolic rates. Furthermore, within this temperature range, minimal effects are observed on healthy cells.[231,232] Together with MRI, activity and site specificity can be readily monitored. Hyperthermia also has the advantage of being used together with chemotherapy or radiotherapy. Therefore, thermo-chemo/radiotherapy probably has a great future in cancer therapy.[233] The overall working mechanism of hyperthermia is shown in Fig. 8. Various IONPs have been developed and administered successfully at tumor site with enhanced heating efficiency. Albarqi *et al.* developed nanoclusters comprising of Zn and Mn-doped IONPs encased in PEG-PCL polymeric NPs. The nanocluster system exhibits enhanced heating efficiency and tumor targeting after administration. These nanoclusters under an AMF, raised the intratumoral temperature beyond 42 °C, successfully suppressing prostate cancer.[234] Similarly, Albarqi *et al.* studied systemically delivered magnetic hyperthermia in ovarian cancer. These nanoclusters, composed of Co- and Mn-doped IONPs encapsulated in PEG-PCL, showing enhanced accumulation in ovarian cancer following intravenous administration and increase intratumoral temperatures up to 44 °C.[235]

An innovative method is introduced to target metallic NPs to glioblastomas by exploiting glucose transporters (GLUT) over-expressed on glioblastoma microvasculature endothelial cells, particularly GLUT1. Caro *et al.*, studied IONPs functionalized with glucuronic acid to promote GLUT-mediated transcytosis, enhanced by inducing mild hypoglycemia. This metabolically driven active targeting approach has demonstrated unprecedented efficacy in directing metallic NPs to glioblastomas. These IONPs, designed as magnetic hyperthermia (MH) mediators, are employed in a preclinical study on MRI-tracked MH therapy following intravenous administration. The results indicate a significant delay in tumour growth. These findings demonstrated unparalleled efficiency in targeting glioblastoma and established a foundation for developing alternative therapeutic strategies to combat this aggressive cancer.[236]

Similarly, theranostic nanoplatforms have shown potential in enhancing tumour treatment efficacy; however, challenges persist in monitoring critical stages and signal durability. Kong *et al.* investigated multi-chambered core/shell MNPs (MC-MNPs) as versatile nanocarriers for drugs and imaging agents. The core comprised of amphiphilic copolymers, while the shell consisted of hydrophilic MIONPs. The nanocarriers' cavities encapsulate desalinised doxorubicin and coumarin 6 separately, with chitosan as an outer encapsulation layer. MC-MNPs exhibited gradient-degraded and steady-released controllability within the tumour environment. The study elucidated real-time accumulation patterns and continuous diagnostic signals of the nanocarriers through fluorescence imaging and T_2-weighted MRI, conducted before and after hyperthermia in targeted tumours under an alternating magnetic field. Consequently, MC-MNPs demonstrate potential for continuous monitoring and guidance of tumour treatment.[237]

4.1 Heating mechanism of magnetic NPs

The mechanism of heating of IONPs during magnetic hyperthermia depends on whether they are ferromagnetic, ferrimagnetic, or super-paramagnetic NPs. The heat dissipation of

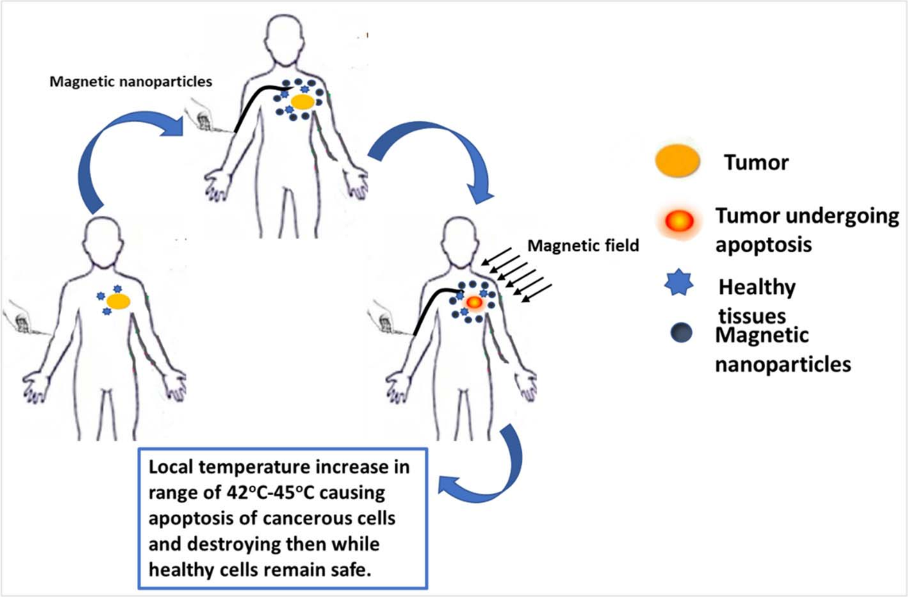

Fig. 8 Working mechanism of hyperthermia.

the NPs takes place by different mechanisms, which are described below.

4.1.1 Hysteresis loss. In ferro- and ferri-magnetic materials, the heating mechanism is based on hysteresis loss. These materials are multi-domain in nature and possess some magnetization even after the removal of an external magnetic field, that is, they have higher coercivities.[238] In the case of ferromagnetic NPs, the magnetic moments of the particles are arranged parallel to each other, thus leading to a net magnetic moment and low energy. In the presence of an external magnetic field, these NPs become either unidirectional to that of the applied field or arranged against the applied field (anti-ferromagnetic materials). Ferrimagnetic NPs consist of magnetic moments that are non-parallel to each other at some points with different magnitudes.[239]

When an external magnetic field is applied to IONPs, the magnetic domains align in the direction of the field. Eventually, a saturation point is reached, where all domains become parallel to the applied field, and the magnetization at this stage is referred to as saturation magnetization (M_s).[240] Beyond this point, magnetization remains constant. After the external magnetic force is removed, the remaining magnetization in the material is termed remanent magnetization (M_r). Owing to this remanent magnetization, a specific level of magnetic field intensity is needed to reverse the field back to zero magnetization.[241] The persistence of magnetization even after the removal of the external field helps these materials to be used as permanent magnets. The specific field to undo the alignment of the magnetic domains in the reverse direction is called the coercivity or coercive field. The work done by this field in overcoming the opposing force produced by atoms or particles results in energy loss in the form of heat energy, which is known as hysteresis loss and is given by the area under the hysteresis loop.[242] The hysteresis loop of a ferromagnetic material in comparison to paramagnetic and superparamagnetic magnetic materials is shown in Fig. 9a. From this figure, it can be easily seen that the curves for ferro-materials have high values of remanent magnetization and coercivity. The energy dissipated as heat is depicted by the area of the loop, that is, the larger the area, the greater the energy dissipated.

Bulk ferromagnetic materials are composed of specific regions that possess definite magnetic moments that are aligned in a different direction from those in another region.[245] These regions are called domains and are separated by thin domain walls. When an external field is applied, these domains vanish and align themselves with the direction of the applied field. Conversely, in super-paramagnetic materials, there are no domain walls, and instead of being multi-domains, they exist as single domains.[246] IONPs also dissipate heat in the form of eddy current losses. This type of heating mechanism is associated with larger particles of centimeter size and occurs when the magnitude of the applied magnetics flux fluctuates, and the resultant resistance causes dissipation of thermal energy to the surroundings. Since magnetic hyperthermia is based on nano-sized particles, these types of materials are not suitable for magnetic hyperthermia.[246]

4.1.2 Super-paramagnetic nanomaterials (SPNMs). SPNPs are single-domain IONPs that behave like single magnets because all their magnetic domains are aligned in one direction. Ferro- and ferri-magnetic materials show super-paramagnetism when their sizes are in the nano range, and they possess magnetic domains arranged in a single direction because of their small size. Unlike ferro- and ferrimagnetic materials, they do not retain their magnetization after removal of an external magnetic field in the form of M_r. This property allows them to be effectively used in biomedical applications, especially magnetic hyperthermia. In magnetic hyperthermia, the heat produced by these particles undergoes two types of mechanisms: Brownian and Néel relaxations.[242]

The magnetocaloric effect (MCE) refers to the temperature change in magnetic materials when exposed to variations in magnetic fields, resulting in either heating or cooling. Its was first discovered by Warbourg in 1881.[247] The parameters affecting MCE include size, shape, composition, and shell–core

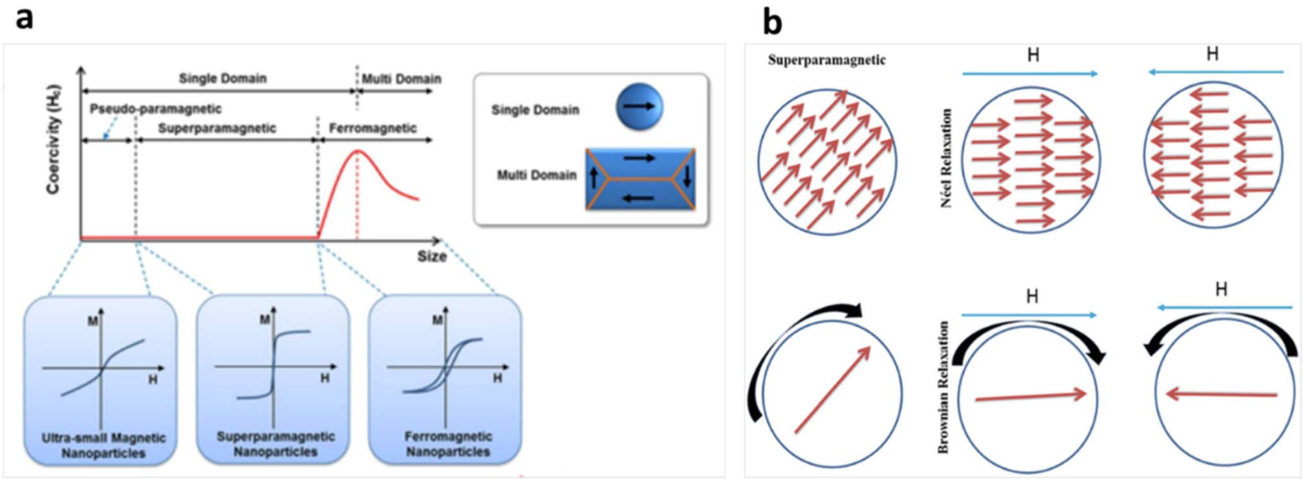

Fig. 9 Hysteresis loop (a) Brownian relaxation USM NPs, superparamagnetic, and ferromagnetic nanoparticles (b) of superparamagnetic NPs. Copyright 2017, Springer Nature.[243,244]

structure, which significantly influence the magnetic properties of IONPs, such as saturation magnetization, coercivity, blocking temperature, and relaxation time.[248] Size plays a crucial role in determining the MCE of IONPs. As the particle size decreased, the surface-to-volume ratio increased, leading to enhanced surface effects and altered magnetic behavior. This can result in a change in the Curie temperature and magnitude of the MCE. Similarly, the shape of IONPs can have a significant impact on their magnetocaloric properties. Different shapes, such as spheres, cubes, or rods, can lead to varying magnetic anisotropies and surface effects, which in turn affect MCE.[248] The composition of IONPs is another critical factor that determines their magnetocaloric properties. For instance, in $Mn_{1-x}Cu_x$-CoGe compounds, substituting Cu for Mn leads to the coupling of magnetic and structural degrees of freedom, resulting in a first-order magneto structural phase transformation and a giant magnetocaloric effect over a wide temperature range.[249]

4.1.2.1 Brownian relaxation. Under the influence of an alternating magnetic field, the magnetic moments of IONPs arrange themselves in the direction of the applied field, and the magnitude of the magnetization increases until saturation is attained. After saturation, the field is reversed to bring the magnetization back to zero, and the magnitude of this reversed field depends on the energy barrier produced by the IONPs to oppose this reversion. Nanosizing of the particles significantly reduced the energy barrier. Single-domain super-paramagnetic IONPs undergo thermal fluctuations, which result in different relaxation processes.[250,251]

When the magnetic field is reversed, there is insufficient rotational friction associated with the particles, which then undergo rotation and change their direction with respect to the reversed field. In such cases, rotational friction is the measure of the proposed energy barrier. This kind of relaxation mechanism is termed Brownian relaxation, where the particles undergo complete rotation with no change in their magnetic moments.

Fig. 9b shows Brownian relaxation of superparamagnetic IONPs. The bold arrow around the particles indicates the rotational relaxation of the entire particle with respect to the magnetic field. Brownian relaxation emits thermal energy to the surroundings owing to shear stress and causes heating the cancer cells during magnetic hyperthermia. The relaxation time for Brownian relaxation (τ_B) is given by

$$\tau_B = \frac{(3\eta V_H)}{(k_B T)} \tag{1}$$

where η is the = viscosity of the medium, V_H is the hydrodynamic volume of the IONPs, k_B is the Boltzmann constant, and T is the temperature (Kelvin).

In the case of Brownian motion, the anisotropy of a IONP is strong enough to overcome the frictional force offered by the viscosity of the medium. Under an AC magnetic field, the magnetic moment remains unchanged and adheres to the crystal axis. From eqn (1), one can see that the Brownian relaxation time depends mainly on the viscosity of the medium and hydrodynamic volume of the particles. Thus, Brownian relaxation is dominant for larger volumes and lower viscosities. The term hydrodynamic volume refers to the volume of the IONPs when it is under the effect of other particles in the medium and any associated coating agents or surfactants.[242,252,253]

4.1.2.2 Néel relaxation. Superparamagnetic IONPs are single-domain particles, which have specific magnetic dipoles and behave as single magnets on the nanoscale as compared to the bulk form. In the absence of an external field, crystalline anisotropy (for spherical particles) and shape anisotropy (for nonspherical IONPs) determine the respective orientation of the magnetic dipoles. When the applied AC magnetic field is strong enough to overcome the respective anisotropy, the dipole moments orient themselves in the direction of the applied field without any change in the positions of the particles, that is, no rotational changes occur. The relaxation associated with the particles attaining an equilibrium position is Néel relaxation.

The Néel relaxation time is sufficiently short to change the positions of all the particles and only causes changes in the magnetic moments of the particles. The expression for the Néel relaxation time (τ_N) is given below:

$$\tau_N = \tau_0 \ \exp \ \frac{K_U V_M}{k_B T} \tag{2}$$

τ_0 = attempt time, K_u = anisotropy constant, V_M = primary volume of the IONPs, T = temperature (Kelvin), and k_B = Boltzmann constant.

From eqn (2), the Néel relaxation depends strongly on the anisotropy constant of the IONPs, as well as their primary volume. The primary volume of a particle is considered not the hydrodynamic volume, as there is no physical change occurring in the position of the particle but only in its dipole change. Néel relaxation is dominant for small particles and higher viscosities. When the medium is more viscous, it is difficult for the particle to undergo rotational change because of the higher energy barrier produced.

The overall relaxation of the NPs involves both processes, that is, Néel and Brownian relaxation, occurring simultaneously. Their relative contributions depend on the actual relaxation times involved, and the mechanism with the shorter time scale is always predominant. The overall relaxation time when both processes occur simultaneously is shown in eqn (3):

$$\tau = \frac{\tau_B \tau_N}{\tau_B + \tau_N} \tag{3}$$

Magnetic fluids used in magnetic hyperthermia treatments respond to alternating fields in the form of Néel and Brownian relaxations. The measurement of the given response is given in the form of a spectrum called the dynamic magnetic spectrum (DMS). Depending on the nature of the ferrofluid components, peaks appear in the spectrum for both types of relaxation.[243] If the ferrofluid consists of non-interacting NPs, they then undergo one kind of relaxation, either Néel or Brownian relaxation, and exhibit a single peak. On the other hand, if the ferrofluid consists of interacting IONPs and there is an uneven size distribution, they will undergo both relaxation processes simultaneously, giving two peaks, one for each.[254] For magnetic hyperthermia, IONPs that undergo Néel relaxation are favored over those that undergo Brownian relaxation because the latter is viscosity dependent. When IONPs are sent to an infected area, changes in the viscosity of the medium surrounding the cells can occur. This situation can hinder the free rotation of the IONPs and so prevent Brownian relaxation.[242,250,252,253]

4.1.2.3 Specific absorption rate. As discussed in the previous section, the relaxation time for IONPs undergoing Néel and Brownian relaxation is responsible for the dissipation of heat because of the faster oscillation under an AC magnetic field. The power dissipated by the IONPs is given by eqn (4):

$$P = \mu_0 x'' f H^2 \tag{4}$$

where P = the heat dissipation value, μ0= permeability of free space, f = AC magnetic susceptibility, f = frequency of the applied AC magnetic field, H = strength of the applied AC magnetic field.

The power dissipation of IONPs during magnetic hyperthermia is associated with other parameters. SAR is the most important parameter. Other important parameters are the SLP and ILP. Moreover, the specific absorption rate is a quantitative measurement of the heat produced during the relaxation processes. It is given in W g^{-1} and is equated as

$$\mathrm{SAR} = C\frac{\Delta T}{\Delta t} \tag{5}$$

where, C = specific heat capacity, $\frac{\Delta T}{\Delta t}$= initial slope of the time-dependent heating curve.

SAR also depends on the AC magnetic field and the applied frequency of the field. This is evident from the power dissipation equation, where there is a direct relationship between the heat dissipated and the magnitude and frequency of the applied magnetic field.[243] The magnetic field cannot be applied beyond a certain threshold limit because it causes several harmful effects on the surrounding healthy tissues. Therefore, there is an experimental threshold level for the magnetic field and its frequency (Hf), that is, 5×10^9 A m^{-1} s^{-1}. In addition, the size of the IONPs also plays an important role in obtaining the maximum SAR value.[242,255] The optimum size of IONPs for obtaining the maximum SAR value was investigated by Hergt *et al.*, who found that the IONPs size at the transition point between super-paramagnetism and ferromagnetism is the optimum size. There are also many other factors that can affect the SAR value, such as composition, modifications, and size distribution.[256]

Consequently, Pankhurst *et al.* proposed a different parameter that is independent of the frequency and magnitude of the applied field. Using this parameter, it is possible to achieve a more accurate comparison of heat dissipation by different superparamagnetic nanoparticles. This parameter is known as ILP. It is based on the optimized value of SAR at a specific frequency and field.[257]

4.2 Effect of magnetic hyperthermia on cancer cells

There are two types of cell death processes in our body: apoptosis and necrosis. Apoptosis is a natural process of controlled cell death, while necrosis is an induced process (due to radiation, chemicals, injury, diseases, or lack of blood flow) of cell death, which may result in spillage of intracellular materials in the surrounding area, thus causing inflammation.[258] Necrosis is a fatal process that causes severe effects and even death. Healthy cells can tolerate temperatures in the 42–45 °C range, whereas tumor cells undergo apoptosis in this temperature range. Above 46 °C, necrosis occurs. Therefore, necrosis is not a preferred treatment for cancer, as magnetic hyperthermia-induced apoptosis is much safer.[259] Unlike normal cells and tissues, cancer cells have more blood flow and faster metabolic processes. The blood flow helps to dissipate the excess energy thus maintaining an optimum temperature for the cancer cells to undergo mitosis.[260] It has been observed that the blood flow in cancer cells decreases when magnetic hyperthermia is applied at 42 °C, while the blood flow of healthy cells is increased significantly. Owing to the decrease in the blood flow for cancer cells, heat dissipation is decreased, thereby causing the cancer cells to undergo apoptosis and become damaged. However, normal cells can survive at this temperature because of the increased rate of heat dissipation.[254,261,262]

Another factor responsible for apoptosis damage in cancer cells is mitosis. As cancer cells can divide rapidly and uncontrollably, most cells remain in the mitosis stage, where they are more susceptible to apoptosis under the influence of magnetic hyperthermia. The physiological differences between normal healthy cells and cancer cells lead to a more profound effect of magnetic hyperthermia. Several attempts have been made to further improve the heating process of magnetic hyperthermia while having no harmful effect on healthy surrounding tissues and cells.[242,251,263]

4.2.1 Factors affecting the heating efficiency of magnetic nanoparticles

4.2.1.1 AC magnetic field. The dissipated energy (P) is directly proportional to the square of magnetic field (H^2) and the frequency and is given in eqn (4).

Therefore, the SAR value is directly proportional to the square of the magnetic field (H^2), as it is the quantitative measure of the heat/power dissipation. The greater the field strength, the higher the SAR value. As discussed earlier, in biomedical applications, the field strength should not exceed a certain threshold limit. If this situation occurs, it leads to heating of the surrounding nonmagnetic tissues because of the induced eddy loss, and this will cause injury to the healthy tissues. Therefore, it is important to maintain the product of the field strength and frequency within a limited range, which will be the optimum condition for magnetic hyperthermia treatment.

4.2.1.2 Anisotropy. When IONPs are under the influence of an external magnetic field, two different situations can occur, as discussed in the previous sections. In one case, the magnetic field strength is strong enough to rotate the magnetic moment of the IONPs or even rotate the particles entirely. If the energy barrier associated with the magnetic moment rotation is small, then the applied magnetic field can change the axes of magnetic moments; such rotations are known as Néel's rotations. However, if the barrier energy overcomes the field, then all the particles rotate depending on various factors, such as viscosity and size. These rotations are associated with Brownian rotations. The energy barriers associated with the rotation of the magnetic moment are referred to as anisotropy energies. Consequently, it is the anisotropy energy that chiefly determines whether particles are operating under Néel or Brownian relaxation.

Anisotropy is mainly responsible for maintaining the spins of the IONPs in *a* direction associated with nonspherical atomic orbitals. The anisotropy energy is given by eqn (6):

$$E = KV\sin^2\theta + \text{higher order terms} \tag{6}$$

where K is the anisotropy constant, V is the volume of the particle, and θ is the angle between the particle magnetization and the easy magnetization axis of the particle. Because the higher-order terms are very small compared with the first term, they can be ignored.[264]

From the above equation, the anisotropy energy depends directly on the anisotropy and volume of the IONPs. SPNPs are single-domain IONPs with small size and thus have small anisotropy energy, which allows them to rotate freely in the absence of an external magnetic field, resulting in zero net magnetization. Anisotropy plays an important role in both the Néel relaxation and SAR values, and it should be controlled accordingly:

From the above eqn (2), the anisotropy constant is important and if kept constant it will depend on the size/volume of the IONPs. If the measuring time (τ_m) is greater than Néel relaxation time (τ_N), *i.e.*, $\tau_m > \tau_N$, then the net magnetization will return to zero. Conversely, if τ_m is less than the Néel's relaxation time $\tau_m < \tau_N$, then the magnetization will not have sufficient time to relax back and so will have a non-zero value.

An increase in relaxation time does not always increase the SAR value. From the eqn (7) for susceptibility (x'') given below, the SAR value is at a maximum when $\omega\tau = 1$ as the SAR value depends on x''.

$$x'' = [\omega\tau/1 + (\omega\tau)^2]x^0 \tag{7}$$

Therefore, an increase in anisotropy will increase the relaxation time and therefore also increase the value of $\omega\tau$, *i.e.*, $\omega\tau > 1$. As a result, the SAR value will decrease as shown by eqn (8).

$$\text{SAR} = \frac{\pi\mu^0 x'' f H^2}{\rho} \tag{8}$$

From eqn (8) the SAR value depends on both the susceptibility and the frequency.[250,265,266]

4.2.1.3 Particle size. The size of IONPs also plays an important role in maintaining the heat generation process. In fact, size is the parameter that determines which type of mechanism will be responsible for the dissipation of energy in the form of heat, the quantization of which is known as the specific SAR. Heat generation mainly takes place through relaxation mechanisms, that is, Brownian or Néel relaxation, and from hysteresis loss. The latter occurs for large particles (~4100 nm), and these IONPs cannot be used in hyperthermia because the large particles are unable to penetrate the infected tissues, and their colloidal solutions are unstable. When the particle size is reduced below 15 nm, the regime of single domain superparamagnetism comes into play. In such a case, the Néel and Brownian relaxation processes dominate, and once again, the decision as to which mechanism will dominate will depend on the size range.

Fig. 10 illustrates how anisotropy affects relaxation time and SAR. The lower plot shows the Brownian, Néel, and effective relaxation times for particles with anisotropy constants (κ) of 40, 25, and 10 kJ m^{-3}. The shaded area highlights the optimal relaxation times (where $\omega\tau = 1$) for achieving SAR within the 100–300 kHz frequency range. In the upper plot, SAR is depicted as a function of particle diameter at 150 kHz for κ values of 40, 25, and 10 kJ m^{-3}. SAR is represented in arbitrary units. As discussed previously, the SAR value depends not only on the particle size but also on the magnetic field and frequency and is maximum for $\omega\tau = 1$. The mainly reported frequency range used for hyperthermia is 100–300 kHz, which results in a relaxation time of the order of 10^{-6} s and falls in the Néel relaxation regime, whereas for $\tau = 10^{-5}$ it falls in the Brownian relaxation regime. Thus, for hyperthermia applications, IONPs with sizes less than 15 nm undergo Néel relaxation, and the anisotropy of the system must be greater than the thermal energy. However, if the anisotropy is intermediate, then it will not be sufficient to generate heat through Néel relaxation. In practice, the size

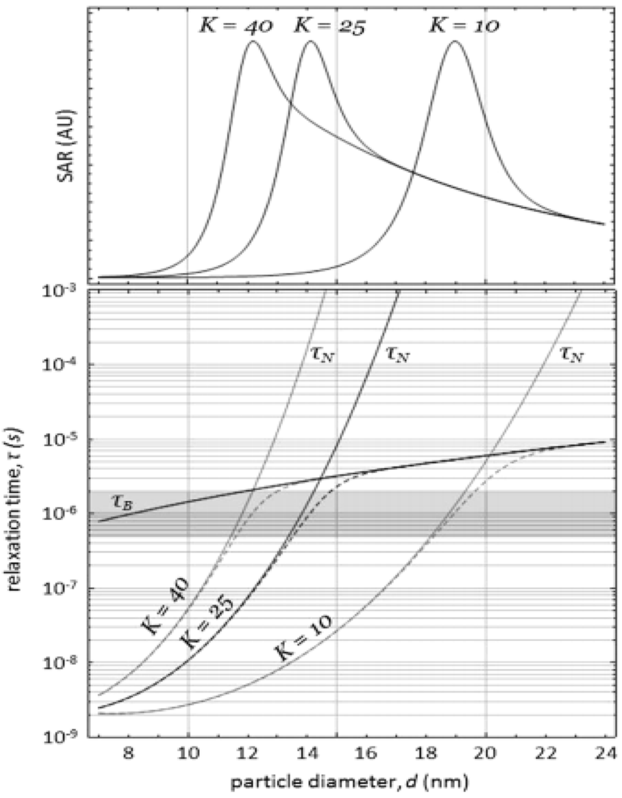

Fig. 10 Effect of anisotropy on relaxation time and SAR. Copyright 2014, Elsevier.[194,250]

distribution of IONPs often exhibits a broad range, encompassing both single- and multi-domain IONPs. Achieving and maintaining a narrow size distribution of IONPs can be challenging.

4.2.1.4 Saturation magnetization (M_s). M_s is another important factor that affects the heating efficiency of magnetic NPs in magnetic hyperthermia. Magnetic hyperthermia is best associated with high magnetization, which results in a higher SAR value.[265]

Essentially, the saturation magnetization is inversely proportional to the ratio of the radius of the disordered spin layer to the radius of the nanoparticles. This ratio increases as the size of the IONPs decreases, as indicated in eqn (9).[267]

$$M_s = M_{s_b}\left[\frac{(r-d)}{r}\right]^3 \tag{9}$$

where d = thickness of the particle's surface exhibiting disordered spins, M_{s_b} = bulk M_s.

Rosensweig *et al.*[268] have shown that there is a relationship between the SAR with and the saturation magnetization according to eqn (10):

$$\mathrm{SAR} = 4.1868\pi{\mu_0}^2\frac{\varphi {M_s}^2 V}{1000KT}{H_0}^2\nu\frac{2\pi V\tau}{1+2\pi V\tau^2} \tag{10}$$

φ = volume fraction of magnetic NPs, ν= magnetic volume of magnetic NPs, H_0 is the magnetic field intensity, ν= frequency, τ = relaxation time, and M_s = saturation magnetization.

This equation shows that the SAR value strongly depends on saturation magnetization.

Despite all advantages, IONPs face the problems of biotoxicity and hemocompatibility.[268] Being hydrophobic in nature, agglomeration is also a serious concern, which makes them detectable by the bio-immune system of the body; hence, they are removed from the cancer site before being used.[269] To address these issues, many agents, including polymers and other biocompatible materials, have been used to coat IONPs.[270] Coating with these agents makes them both bio- and hemocompatible, while preventing agglomeration and thus reducing biotoxicity to a normal level.[271] Table 3 lists the various IONPs reported in the literature. Furthermore, different strategies, such as the core shell concept, combination of hyperthermia with other techniques, and doping with other metals, have been employed to minimize the unwelcome side effects of ferrites.

Transition elements have been widely used as tuning agents in certain types of ferrites. Pardo *et al.*[284] have explored the effects of cobalt, manganese, and zinc on the magnetic properties of ferrites. Different dopant concentrations resulted in different magnetic properties. Cobalt ferrite is a type of spinel ferrite and is the only hard magnet in this family. It exhibited the highest saturation magnetization and coercivity. All synthesized IONPs were superparamagnetic and biologically stable in aqueous media for up to 72 h. The heating efficiency of these particles for use in magnetic hyperthermia was demonstrated by their enhanced specific absorption rate (SAR), for example, 100 W g^{-1} for cobalt ferrite. Co based IONPs show potential applications in magnetic hyperthermia due to their high effective heating and higher specific power loss.[290] These NPs can form growing chains under alternating magnetic fields, leading to complete tumor regression and improved survival in animal models.[291] However, Co is toxic when ingested in large amounts, with potential effects on the cardiovascular system, lungs, and hearing. Manganese, which is also an essential trace element, can be toxic in excess. It is primarily associated with neurotoxicity, causing a disorder similar to Parkinson's disease known as Manganism.[292,293] Further research is needed to fully understand the long-term effects of these metals and optimize their use in cancer therapy while minimizing potential risks.

Core/shell IONPs have recently been used in the biomedical field owing to their several advantages, including compatibility

Table 3 SAR, IPL, and M_s of IONPs with different coatings

NPs	Coating	Size (nm)	M_s (emu g^{-1})	SAR (W g^{-1})	ILP (nH m^2 kg^{-1})	Ref.
Iron/iron oxide core shell	—	78	200	900	—	272
Mn–Zn–Fe_2O_4	Hyaluronic acid	—	—	—	—	273
Fe (CO_x)	Oleyl amine	9–18	164	278	1.52	274
Zn–ferrite	Oleic acid/oleyl amine	6.1–11.1	16.1	69.7	0.043	275
Yttrium ferrite	—	—	—	194	1.85	276
Zn–Mn–Fe_3O_4	PEG	10–15	81	25.1		277
Fe_3O_4/Co–Fe_2O_4	—	—	—	450	—	278
Zn–ferrite/chitosan	Chitosan	200	103	140	0.4	279
$CoFe_{1.95}Dy_{0.05}O_4$	CMC	15–25	51.8	494		280
Mn–ferrite	—	—	61	90	—	281
$Co_{0.6}Fe_{2.4}O_4$	Oleic acid	8.1	88	40.4		282
Co–ferrite	Oleic acid	—	—	297.4	—	283
$Zn_{0.25}Co_{0.29}Mn_{0.21}Fe_{2.25}O_4$	Oleic acid	8.6	98	97		284
Zn–Mn–ferrite	PEG	—	81	46	1.0	277
$Co_{0.6}Zn_{0.05}Fe_{2.25}O_4$	Glycine	14–19	81	52.6		285
$Mn_{0.5}Zn_{0.5}Fe_{1.97}Gd_{0.025}$	—	12	48	146		286
Citrate capped IONPs	Citric acid	—	74	16.74		287
Zn–Co ferrite	Oleic acid	7	90	19		288
Iron oxide nano discs	CTAB	12	60	125		289

with the target site by tuning the core of the IONPs with different coating agents.[294] In the case of invasive hyperthermia and drug delivery, these particles help to manage drug release at the target site, thus preventing unnecessary drug loss.[295] Simeonidis *et al.*[272] studied the interaction between the core and shell of IONPs, in which the core is of iron, while the shell consists of an iron-oxide layer. Different ratios of the core and shell radii were investigated, and the results were compared with those of IONPs having a fully metallic core and complete oxide shell. The saturation magnetization proved to be the maximum for the sample having a large proportion of iron core, that is, 200 A m^2 kg^{-1}, while the specific absorption rate (SAR) was maximum for the almost pure iron oxide core sample with a small iron content resulting from the decomposition of iron oxide. The SAR value for a particle size of 78 nm was exceptionally high, that is, 900 W g^{-1}, illustrating the remarkable heating efficiency. Similarly, Vinas *et al.*[278] also described a favorable core/shell approach consisting of spinel ferrite, that is, Mn-ferrite and Co-ferrite as hard shells surrounding an iron oxide core. The interaction between the core and shell gives rise to better biocompatibility, resulting in a promising heating efficiency for magnetic hyperthermia. Fe_3O_4/Mn–Fe_2O_4 core shell IONPs are soft in nature and thus show low coercivity and magnetization values. The associated specific absorption rate was also low for this material. On the other hand, Fe_3O_4/Co–Fe_2O_4 core–shell IONPs are hard magnets that exhibit a considerable amount of magnetization and coercivity. The specific absorption rate (SAR) increased remarkably for this sample, and at a frequency of 765 kHz, Fe_3O_4/Co–Fe_2O_4 had a SAR value of 450 W g^{-1}. Ravichandran *et al.*,[296] examined spinel cobalt ferrite NPs covered with a gold (Au) core shell for biocompatibility and found that these materials have reduced toxicity.

The core–shell structure allows for the combination of different materials with complementary properties, enhancing the performance of IONPs in magnetic hyperthermia. For instance, a study on FePt@IONPs core–shell demonstrated that this structure promotes the formation of vortex-like intraparticle magnetization, reducing dipolar interactions between neighbouring IONPs while enhancing relaxivity during MRI scans.[297] This dual functionality improves both diagnostic and therapeutic capabilities. Interestingly, the compositions of the core and shell can be tailored to optimize specific properties. $Zn_xMn_yFe_zO_4@\gamma\text{-}Fe_2O_3$ and $Zn_xCo_yFe_zO_4@\gamma\text{-}Fe_2O_3$ core–shell IONPs showed that the contrast in anisotropy between the core and shell materials affects the heating efficiency, as measured by specific power absorption.[298] This suggests that careful selection of core–shell materials can enhance the performance of IONPs in magnetic hyperthermia. For example, Fe_3O_4@Alg-GA NPs with D-galactosamine ligands on the alginate shell demonstrated enhanced cellular uptake and excellent hyperthermic efficacy in HepG2 cells.[299] Additionally, the use of a silica coating on the $\gamma\text{-}Fe_2O_3$ cores enabled the grafting of oligonucleotides for targeted release upon magnetic hyperthermia activation.[300]

Wang *et al.*[273] have investigated a ternary ferrite system consisting of iron oxide, manganese, and zinc capped with hyaluronic acid (to avoid agglomeration) for radiotherapeutic applications. They also injected the IONPs into a biopolymer consisting of polyethylene glycol and polycaprolactone (PEG-PCL), whose function was to maintain biocompatibility within the body and to prevent dispersion of the particles to other sites. The combined method was subjected to both *in vitro* and *in vivo* analyses against A549 type cancer cells and caused a reduction in the size of a tumor by 49.6% in the *in vitro* study.

Chemotherapy and radiotherapy are commonly used in combination with hyperthermia as cotherapies. Takook *et al.* studied this approach of combined therapies to treat deep-seated head and neck tumors. The addition of hyperthermia to these conventional therapies may be particularly beneficial for children with brain cancer, where late side effects are a concern.[301] Similarly, Lassche *et al.*, studied whole-body hyperthermia in combination with systemic chemotherapy for metastasized solid malignancies, although the additive value remains speculative due to the absence of phase III trials.[302] Interestingly, recent research has focused on combining hyperthermia with immunotherapy, opening up new possibilities in cancer treatment.[303] This multidisciplinary synergistic approach has demonstrated effectiveness, and the underlying mechanisms are being gradually explored. Additionally, the combination of hyperthermia with anti-cancer drugs or natural products has been investigated to overcome limitations such as increased heat shock protein production.[304]

Doping and co-doping ferrites with transition metals brings about different properties, and by varying the compositions, it is possible to tune the properties to a desired level. Etamadi *et al.*[275] have synthesized iron oxide doped with transition and non-transition elements (Fe, Mg, and Zn) by a hydrothermal process using oleic acid and oleylamine as surfactants in a 1 : 4 ratio. Crystallites of varying sizes in the range of 6.1–11.1 nm were formed. Zinc ferrite led to a maximum saturation magnetization of 16.1 emu g^{-1} as compared to other dopants, and its coercivity was 43 Oe. Hyperthermia studies have shown the heating efficiency of IONPs as ferrofluids in treating cancer. The SAR was maximum for zinc ferrite (69.7 W g^{-1}) with an intrinsic loss power of 0.043 nH m^2 kg^{-1}. Doping of ferrites with rare-earth metals has also shown enhanced performance in *in vivo* cancer studies. Kowalik *et al.*[276] have investigated the doping effect of yttrium and its application in magnetic hyperthermia. Ferrite, with 0.1% yttrium, was best suited for this purpose and exhibited a significant heating ability. The SAR was 194 W g^{-1} and the intrinsic ILP was 1.85 mH^2 kg^{-1} for an alternating magnetic field of 16 kA m^{-1} and a frequency of 413 kHz. *In vitro* hyperthermia studies were undertaken, and 35 μg mL^{-1} of the sample caused a 77% reduction in $4T_1$ cell viability.

De Mello *et al.*[277] worked on Co-doping of Zn–Mn-ferrite synthesized by a coprecipitation method and coated by polyethylene glycol (PEG). Co-doping increased the saturation magnetization to a maximum value of 81 emu g^{-1}. However, in the case of hyperthermia, manganese-doped ferrite has the maximum SAR and ILP values of 46 W g^{-1} and 1.0 nH m^2 kg^{-1}, respectively. In another attempt, the doped MFe_2O_4 (M = Co, Fe, or Mn) was prepared hydrothermally using cotton as a template. The cotton template was removed by calcinating the samples, and a change in morphology was observed for Fe and Mn ferrite, but Co ferrite retained its spinel structure. The observed SAR and magnetization values for manganese ferrite were 90 W g^{-1} and 61 A m^2 kg^{-1}, respectively, as calculated by Mendo *et al.*[281]

Polymers play an important role in providing biocompatibility for various drugs and IONPs. They also help to decrease the dosage of drugs by preventing their early release before reaching the target site. Lachowicz *et al.*[279] have reported a facile method for the synthesis of zinc-doped iron oxide coated with chitosan (CCh), which helps create a biocompatible environment for IONPs and reduces cytotoxicity. The core size of the zinc ferrite NPs were found to be approximately 10 nm for a CCh coating, and they obtained a particle size of 200 nm. The $Zn_{0.33}Fe_{2.67}O_4$–CCh sample showed the highest magnetic saturation value of 103 emu g^{-1}, and in *vitro* hyperthermia studies also revealed that the sample is highly stable in biological media. For a sample concentration of 0.18–0.66 mg mL^{-1} of iron, an obvious increase in the heating capacity of this sample was observed. The SAR and ILP were 140 W g^{-1} and 0.4 nH m^2 kg^{-1}, respectively. Nam *et al.*[283] synthesized IONPs of cobalt ferrite using a thermal decomposition method. These IONPs were incorporated into polymers to provide hemocompatibility and lower or eliminate toxicity. The polymers used were oleic acid, poly(maleic anhydride-*alt*-1-octadecene), and oleylamine. Poly(maleic anhydride-1-octadecene) also helped stabilize them in biological media. *In vitro* hyperthermia studies showed important results, and the SAR value was 297.4 W g^{-1} in an applied field of 300 Oe and at a frequency of 450 kHz.

Magnetic nanofluids are also efficient in cancer therapy, and the effect of such nanofluids in the treatment of adenocarcinoma and mammary carcinoma has been studied by Jordan *et al.*[305] Loizou *et al.*[274] reported a multifluidic synthesis method to produce carbon-based IONPs, specifically iron pentacarbonyl [$Fe(CO)_5$], employing oleylamine as a surfactant. This approach yielded iron carbide IONPs with sizes ranging from 9 to 18 nm, exhibiting a saturation magnetization of 164 emu g^{-1}. The study also investigated the heating efficiency of these NPs in magnetic hyperthermia under an alternating magnetic field, revealing a specific absorption rate (SAR) of 278 W g^{-1} and an intrinsic loss power (ILP) of 1.52 nH m^2 kg^{-1}.

5. Critical analysis

IONPs have received a lot of attention because of their potential use in hyperthermia, drug administration, and MRI contrast enhancement. However, several constraints and obstacles prevent their clinical application and efficacy. The specific absorption rate (SAR) of IONPs, a critical parameter determining heating efficiency, varies significantly between studies due to differences in experimental setups, magnetic field strengths (H), and nanoparticle synthesis methods, resulting in non-uniform heating and low-temperature elevation. Furthermore, IONP aggregation and unequal distribution within biological tissues cause localized hot patches and reduced therapeutic efficacy. Surface coatings and stabilizers also affect IONP biocompatibility, which can bring toxicity, and IONPs' incomplete breakdown or excretion poses health hazards such as oxidative stress, inflammation, and organ damage.

Moreover, IONPs also face limited targeted efficiency due to off target binding and removal by the reticuloendothelial system (RES) which remove therapeutic efficacy.

The drug loading capacity of IONPs is similarly limited by their surface area and functionalization processes, resulting in low drug loading efficiency. In MRI applications, IONPs' relaxivity decreases when introduced into complex biological environments such as blood or tissues, whereas their high magnetic susceptibility produces imaging artifacts, especially in high-field MRI systems. Furthermore, variations in synthesis methods, characterization techniques, and experimental conditions pose challenges to reproducibility and scalability, while stringent regulatory requirements and the need for standardized protocols and characterization techniques impede the clinical translation of IONP-based systems.

6. Conclusion, challenges and future perspectives

In recent years, considerable research has been conducted to develop materials with controlled synthesis, such as size, shape, magnetization, and biocompatibility, rendering them suitable for various applications. In this review the three main biomedical applications of IONPs have been discussed in detail: hyperthermia, MR imaging, and drug delivery for tumor diagnosis and treatment. These nanomedicines are magnetically targeted to the desired sites using external fields. To overcome the limitations of agglomeration and detection by immune system, IONPs have been coated with polymers or proteins. MRI contrast agents enable detailed whole-body imaging, aiding in diagnosis and drug delivery monitoring during treatment, whereas hyperthermia provides treatment at targeted sites. The key factor driving the emergence of IONPs in recent years is their multimodal functionality, which allows them to serve as diagnostic and therapeutic agents. By optimizing properties such as magnetization, functionalization, size, and shape, IONPs can effectively image, diagnose, and target affected sites for nanomedicine-based therapy. Surface functionalization through appropriate coating agents forms composites with improved synergistic effects, enhanced stability, reduced toxicity, and enables a target-oriented approach. Size and shape also influence their efficiency in multimodal therapy.

Despite significant research in the field, there are many challenges in fully harnessing the potential of IONPs such as size, aggregation, magnetization, and biocompatibility. IONPs used in hyperthermia, drug delivery, and MR imaging may exhibit dose-dependent toxicity, thus urging for more research to enhance their biocompatibility. Future focus should be on a multimodal approach to create multifunctional agents for theranostic purposes, combining treatment and diagnosis. Many IONPs have been introduced as theranostic agents, offering promising potential for biomedical applications. These agents also have applications in hyperthermia, effectively killing cancer cells through heat generation and magnetic drug delivery. However, enhancing the biocompatibility and biostability of such multifunctional agents remains a significant challenge. IONPs offer a broader range of biomedical applications and robust interdisciplinary research in modern sciences. Exploring beyond established concepts is crucial to precisely define and achieve quantitative functional characteristics of NPs for specific applications. Further investigation in this field is highly desirable to advance biomedical technologies.

For MRI, NPs with size (<5–10 nm) and USPIONs <5 nm are best suited as T_1 while NPs with particle size (>20 nm) as T_2 contrast agents. Surface modification of IONPs with polymers *etc.* further improves their biocompatibility and circulation time. Moreover, particle size in the range of 15–20 nm is optimal for maximum heating efficiency *via* Néel relaxation. In general, SPIONs in the 10–100 nm range with polymer coatings are versatile for all three applications. Optimizing size, surface properties and composition is key for each specific application. Multifunctional NPs combining imaging, hyperthermia and drug delivery capabilities are an active area of research.

Abbreviations

Transition metal oxides	TMOs
Magnetic nanoparticles	IONPs
Superparamagnetic iron oxide	SPIONs
Nanoparticles	NPs
Polyethylene glycol	PEG
Polycaprolactone	PCL
Specific absorption rate	SAR
Chitosan	Ch
Remanent magnetization	M_r
Saturation magnetization	M_s
Computed tomography	CT
Optical imaging	OI
Positron emission tomography	PET
Single-photon emission	SPECT
Iron oxide nanoparticles	IONPs
Magnetic resonance	MR
European Medicines Agency	EMA
Enhanced permeability retention	EPR
Ultra small superparamagnetic iron oxide nanoparticles	USPIONs
Monocrystalline iron oxide nanoparticles	MIONPs
Cross-lined iron oxides	CLIOs
Microparticles of iron oxide	MPIO
Colloidal iron oxide nanoparticle platforms	CIONPP
P-glycoprotein	P-gp
small hairpin RNA	shRNA
Mesoporous silica nanoparticles	MSNPs
Doxorubicin	DOX
Polyethyleneimine	PEI
Porphyrin–metal–organic frameworks	PMOFs
Magnetic gold nanoparticles	MGNPs
Polyethylene glycol	PEG
Poly(D,L-lactide-*co*-glycolic acid):	PLGA
Magnetic microsphere system	MMS

Data availability

Data sharing is not applicable to this article as no new data was created or analyzed in this work.

Conflicts of interest

The authors declare no conflicts of interest.

Acknowledgements

The authors extend their appreciation to the Deanship of Scientific Research at King Khalid University, Saudi Arabia, for funding this work through the Large Groups Project under grant number RGP2/524/45, the Higher Education Commission of Pakistan and Pakistan Academy of Sciences.

References

1 M. Z. U. Abidin, M. Ikram, S. Moeen, G. Nazir, M. B. Kanoun and S. Goumri-Said, *Coord. Chem. Rev.*, 2024, **520**, 216158.
2 V. Harish, M. Ansari, D. Tewari, A. B. Yadav, N. Sharma, S. Bawarig, M.-L. García-Betancourt, A. Karatutlu, M. Bechelany and A. Barhoum, *J. Taiwan Inst. Chem. Eng.*, 2023, **149**, 105010.
3 A. S. Dousari, S. S. Hosseininasab, M. R. Akbarizadeh, M. Naderifar and N. Satarzadeh, *Sci. Hortic.*, 2023, **320**, 112215.
4 S. Singh, *J. Nanosci. Nanotechnol.*, 2010, **10**, 7906–7918.
5 M. Barani, A. Rahdar, M. Mukhtar, S. Razzaq, M. Qindeel, S. A. Hosseini Olam, A. C. Paiva-Santos, N. Ajalli, S. Sargazi, D. Balakrishnan, A. K. Gupta and S. Pandey, *Mater. Today Chem.*, 2022, **26**, 101131.
6 P. Guardia, X. Batlle and A. Labarta, *J. Phys. Chem. C*, 2010, **115**, 390–396.
7 C. Liu and Z. J. Zhang, *Chem. Mater.*, 2001, **13**, 2092–2096.
8 N. Elahi and M. Rizwan, *Artif. Organs*, 2021, 1272–1299.
9 S. Panda, S. Hajra, A. Kaushik, H. G. Rubahn, Y. K. Mishra and H. J. Kim, *Mater. Today Chem.*, 2022, **26**, 101182.
10 L. Kafrouni and O. Savadogo, *Prog. Biomater.*, 2016, **5**, 147–160.
11 X. Liu, H. Jiang and X. Wang, *Biosensors*, 2024, **14**, 100.
12 C. Saka, *Fuel*, 2024, **356**, 129552.
13 A. Rajiv, A. Kapse, V. K. Singh, M. S. Chauhan, A. Awasthi and P. Singh, *Surf. Interfaces*, 2024, **44**, 103628.
14 M. Latorre-Esteves, A. Cortes, M. Torres-Lugo and C. Rinaldi, *J. Magn. Magn. Mater.*, 2009, **321**, 3061–3066.
15 S. Yadav, S. Bhagat, S. Singh and P. K. Maurya, *J. Gerontol., Ser. A*, 2024, **79**, glae197.
16 I. Rosca, I.-A. Turin-Moleavin, A. Sarghi, A.-L. Lungoci, C.-D. Varganici, A.-R. Petrovici, A. Fifere and M. Pinteala, *Int. J. Biol. Macromol.*, 2024, **256**, 128314.
17 R. Nunes, F. Araújo, J. Tavares, B. Sarmento and J. Das Neves, *Eur. J. Pharm. Biopharm.*, 2018, **130**, 200–206.
18 S. K. R. Namasivayam, *Environ. Qual. Manag.*, 2024, **33**, 967–978.

19 D. Miele, L. Malavasi, G. Dacarro, F. Ferrari, S. Rossi, M. Sorrenti, M. C. Bonferoni, G. Sandri and L. Catenacci, *Mar. Drugs*, 2019, **17**, 515.

20 F. Yang, M. Cabe, K. A. Langert and H. A. Nowak, *Pharmaceutics*, 2022, **14**, 95.

21 C. Zhang, R. Wang, L. Zhang, Z. Liu, D. Ning, Q. Li, L. Gao and T. Jiao, *Colloids Surf., A*, 2023, **678**, 132461.

22 C. C. Thong, D. C. L. Teo and C. K. Ng, *Constr. Build. Mater.*, 2016, **107**, 172–180.

23 B. Rezaei, P. Yari, S. M. Sanders, H. Wang, V. K. Chugh, S. Liang, S. Mostufa, K. Xu, J. P. Wang and J. Gómez-Pastora, *Small*, 2024, **20**, 2304848.

24 M. Phadatare, V. Khot, A. Salunkhe, N. Thorat and S. Pawar, *J. Magn. Magn. Mater.*, 2012, **324**, 770–772.

25 M. F. Akhtar, A. Afzaal, A. Saleem, A. Roheel, M. I. Khan and M. Imran, *Med. Oncol.*, 2024, **41**, 53.

26 D. T. K. Dung, T. H. Hai, L. H. Phuc, B. D. Long, L. Vinh and P. N. Truc, *J. Phys.:Conf. Ser.*, 2009, **187**, 012036.

27 J. Mistral, K. T. Ve Koon, L. Fernando Cotica, G. Sanguino Dias, I. Aparecido Santos, P. Alcouffe, N. Milhau, D. Pin, O. Chapet and A. Serghei, *ACS Appl. Nano Mater.*, 2024, **7**, 7097–7110.

28 Y. Ding, Y. Hu, L. Zhang, Y. Chen and X. Jiang, *Biomacromolecules*, 2006, **7**, 1766–1772.

29 S. K. Swain, A. Sahoo, P. Mishra, S. K. Swain and S. K. Tripathy, *Functionalized Magnetic Nanoparticles for Theranostic Applications*, 2024, pp. 69–96.

30 C. Pucci, A. Degl'Innocenti, M. B. Gümüş and G. Ciofani, *Biomater. Sci.*, 2022, **10**, 2103–2121.

31 F. Rodríguez, P. Caruana, N. De la Fuente, P. Español, M. Gamez, J. Balart, E. Llurba, R. Rovira, R. Ruiz and C. Martín-Lorente, *Biomolecules*, 2022, **12**, 784.

32 R. Joppi, V. Bertele, T. Vannini, S. Garattini and R. Banzi, *Br. J. Clin. Pharmacol.*, 2020, **86**, 170–174.

33 X. Jin, P. Makvandi, Y. Tan, J. Huang, Y. Lei, X. Wang, Z. Guo, Y. Xu, R. Esmaeely Neisiany, G. Heidari, A. Cláudia Paiva-Santos, Z. Hua, M. Sillanpää, H. Karimi Male, C. Prakash and Z. Wu, *Eur. Polym. J.*, 2024, **208**, 112891.

34 A. Rong, M. Zhou, M. Zhu, Z. Han, X. Sun and T. Wang, *Wiley Interdiscip. Rev.:Nanomed. Nanobiotechnol.*, 2023, **16**, 1933.

35 R. A. Revia and M. Zhang, *Mater. Today*, 2015, **19**, 157–168.

36 A. Ito, M. Shinkai, H. Honda and T. Kobayashi, *J. Biosci. Bioeng.*, 2005, **100**(1), 1–11.

37 C. L. Partain, *J. Magn. Reson. Imaging*, 2004, **19**, 515–526.

38 P. Storey, *Magnetic Resonance Imaging: Methods and Biologic Applications*, 2006, pp. 3–57.

39 L. Lartigue, P. Hugounenq, D. Alloyeau, S. P. Clarke, M. Lévy, J.-C. Bacri, R. Bazzi, D. F. Brougham, C. Wilhelm and F. Gazeau, *ACS Nano*, 2012, **6**, 10935–10949.

40 C. Westbrook and J. Talbot, *MRI in Practice*, John Wiley & Sons, 2018.

41 W. T. Kimberly, A. J. Sorby-Adams, A. G. Webb, E. X. Wu, R. Beekman, R. Bowry, S. J. Schiff, A. de Havenon, F. X. Shen and G. Sze, *Nat. Rev. Bioeng.*, 2023, **1**, 617–630.

42 C. Yin, P. Hu, L. Qin, Z. Wang and H. Zhao, *Int. J. Nanomed.*, 2024, 9549–9574.

43 A. R. Puente-Santiago and D. Rodríguez-Padrón, *Surface-modified Nanobiomaterials for Electrochemical and Biomedicine Applications*, Springer, 2020.

44 K. Chen, J. Xie, H. Xu, D. Behera, M. H. Michalski, S. Biswal, A. Wang and X. Chen, *Biomaterials*, 2009, **30**, 6912–6919.

45 R. Hachani, M. A. Birchall, M. W. Lowdell, G. Kasparis, L. D. Tung, B. B. Manshian, S. J. Soenen, W. Gsell, U. Himmelreich and C. A. Gharagouzloo, *Sci. Rep.*, 2017, **7**, 7850.

46 S. Xiao, X. Yu, L. Zhang, Y. Zhang, W. Fan, T. Sun, C. Zhou, Y. Liu, Y. Liu and M. Gong, *Int. J. Nanomed.*, 2019, 8499–8507.

47 H. Nosrati, M. Salehiabar, M. Fridoni, M.-A. Abdollahifar, H. Kheiri Manjili, S. Davaran and H. Danafar, *Sci. Rep.*, 2019, **9**, 7173.

48 R. Lin, J. Huang, L. Wang, Y. Li, M. Lipowska, H. Wu, J. Yang and H. Mao, *Biomater. Sci.*, 2018, **6**, 1517–1525.

49 N. Lamichhane, S. Sharma, Parul, A. K. Verma, I. Roy and T. Sen, *Biomedicines*, 2021, **9**, 288.

50 Z. R. Stephen, F. M. Kievit and M. Zhang, *Mater. Today*, 2011, **14**, 330–338.

51 G. Tircsó, E. Molnár, T. Csupász, Z. Garda, R. Botár, F. K. Kálmán, Z. Kovács, E. Brücher and I. Tóth, *Metal Ions in Bio-Imaging Techniques*, De Gruyter Berlin, Germany, 2021, pp. 39–70.

52 E. Peng, F. Wang and J. M. Xue, *J. Mater. Chem. B*, 2015, **3**, 2241–2276.

53 M. Angelakeris, *Biochim. Biophys. Acta, Gen. Subj.*, 2017, **1861**, 1642–1651.

54 M. Amiri, M. Salavati-Niasari and A. Akbari, *Adv. Colloid Interface Sci.*, 2019, **265**, 29–44.

55 Y. Bao, T. Wen, A. C. S. Samia, A. Khandhar and K. M. Krishnan, *J. Mater. Sci.*, 2016, **51**, 513–553.

56 N. Lee, D. Yoo, D. Ling, M. H. Cho, T. Hyeon and J. Cheon, *Chem. Rev.*, 2015, **115**, 10637–10689.

57 R. Ranjbarzadeh, A. Caputo, E. B. Tirkolaee, S. J. Ghoushchi and M. Bendechache, *Comput. Biol. Med.*, 2023, **152**, 106405.

58 H. L. Andersen and M. Christensen, *Nanoscale*, 2015, **7**, 3481–3490.

59 Z. Zhou, L. Yang, J. Gao and X. Chen, *Adv. Mater.*, 2019, **31**, 1804567.

60 V. S. Marangoni, O. Neumann, L. Henderson, C. C. Kaffes, H. Zhang, R. Zhang, S. Bishnoi, C. Ayala-Orozco, V. Zucolotto and J. A. Bankson, *Proc. Natl. Acad. Sci. U.S.A.*, 2017, **114**, 6960–6965.

61 D. Kim, K. Shin, S. G. Kwon and T. Hyeon, *Adv. Mater.*, 2018, **30**, 1802309.

62 R. S. Kumar and M. Karnan, *Int. J. Res. Stud. Comput. Sci. Eng.*, 2014, **1**, 21–28.

63 H. Shokrollahi, A. Khorramdin and G. Isapour, *J. Magn. Magn. Mater.*, 2014, **369**, 176–183.

64 K. L. McMahon, G. Cowin and G. Galloway, *J. Orthop. Sports Phys. Ther.*, 2011, **41**, 806–819.

65 P. Caravan, *Chem. Soc. Rev.*, 2006, **35**, 512–523.

66 D. Ling, W. Park, S.-j. Park, Y. Lu, K. S. Kim, M. J. Hackett, B. H. Kim, H. Yim, Y. S. Jeon and K. Na, *J. Am. Chem. Soc.*, 2014, **136**, 5647–5655.

67 S. Mastrogiacomo, W. Dou, J. A. Jansen and X. F. Walboomers, *Mol. Imaging Biol.*, 2019, **21**, 1003–1019.
68 R. A. Brooks, F. Moiny and P. Gillis, *Magn. Reson. Med.*, 2001, **45**, 1014–1020.
69 H. Chen, J. Yeh, L. Wang, H. Khurshid, N. Peng, A. Y. Wang and H. Mao, *Nano Res.*, 2010, **3**, 852–862.
70 D. Suto, G. Nair, D. Sudarshana, S. Steele, J. Dwyer, E. Beck, J. Ohayon, H. McFarland, A. Koretsky and I. Cortese, *Am. J. Neuroradiol.*, 2020, **41**, 1569–1576.
71 M. O. Besenhard, L. Panariello, C. Kiefer, A. P. LaGrow, L. Storozhuk, F. Perton, S. Begin, D. Mertz, N. T. K. Thanh and A. Gavriilidis, *Nanoscale*, 2021, **13**, 8795–8805.
72 C. Unruh, N. Van Bavel, M. Anikovskiy and E. J. Prenner, *Molecules*, 2020, **25**, 5762.
73 L. Bakhos and M. A. Syed, *Basic Principles of Cardiovascular MRI: Physics and Imaging Technique*, 2015, pp. 271–281.
74 H. B. Na and T. Hyeon, *J. Mater. Chem.*, 2009, **19**, 6267–6273.
75 P. Marckmann, L. Skov, K. Rossen, A. Dupont, M. B. Damholt, J. G. Heaf and H. S. Thomsen, *J. Am. Soc. Nephrol.*, 2006, **17**, 2359–2362.
76 J. Estelrich, M. J. Sánchez-Martín and M. A. Busquets, *Int. J. Nanomed.*, 2015, **10**, 1727.
77 Y. Yan, X. Sun and B. Shen, *Oncotarget*, 2017, **8**, 43491.
78 C. B. Sirlin, D. R. Vera, J. A. Corbeil, M. B. Caballero, R. B. Buxton and R. F. Mattrey, *Acad. Radiol.*, 2004, **11**, 1361–1369.
79 J. Jankovic, *Neurology*, 2005, **64**, 2021–2028.
80 J. Estelrich i Latràs, M. J. Sánchez Martín and M. A. Busquets i Viñas, *Int. J. Nanomed.*, 2015, **10**, 1727–1741.
81 H. Maeda, *Adv. Enzyme Regul.*, 2001, **41**, 189–207.
82 L. Duan, L. Yang, J. Jin, F. Yang, D. Liu, K. Hu, Q. Wang, Y. Yue and N. Gu, *Theranostics*, 2020, **10**, 462.
83 C. Caro, A. Avasthi, J. M. Paez-Muñoz, M. P. Leal and M. L. García-Martín, *Biomater. Sci.*, 2021, **9**, 7984–7995.
84 E. ter Linden, E. R. Abels, T. S. van Solinge, J. Neefjes and M. L. D. Broekman, *Cell*, 2024, **13**, 998.
85 I. Biancacci, B. Theek, D. Moeckel, F. Gremse, S. Von Stillfried, L. Consolino, J. N. May, J. Momoh, M. Baues, A. El Shafei, Y. Shi, Q. Peña, A. Azadkhah Shalmani, K. Benderski, E. M. Buhl, A. Wang, F. Lorenzi, J. Metselaar, W. Hennink, F. Kießling, J. Buyel and X. Bai, *Adv. Sci.*, 2022, **9**, 2103745.
86 J. A. C. M. Goos, K. Mandleywala, S. Puttick, T. R. Dilling, J. F. Quinn, A. Cho, T. P. Davis, W. S. Price, M. Davydova, J. S. Lewis, A. Gupta, L. M. Carter and M. R. Whittaker, *Theranostics*, 2020, **10**, 567–584.
87 H. Lee, D. B. Kirpotin, E. Geretti, I. Krop, C. X. Ma, T. J. Wickham, S. J. Blocker, P. N. Munster, K. Campbell, K. D. Miller, D. F. Gaddy, S. C. Leonard, V. Moyo, B. A. Siegel, A. F. Shields, P. M. Lorusso and B. S. Hendriks, *Clin. Cancer Res.*, 2017, **23**, 4190–4202.
88 Y. Zi, K. Yang, J. He, Z. Wu, J. Liu and W. Zhang, *Adv. Drug Delivery Rev.*, 2022, **188**, 114449.
89 H. Gavilán, S. K. Avugadda, T. Fernández-Cabada, N. Soni, M. Cassani, B. T. Mai, R. Chantrell and T. Pellegrino, *Chem. Soc. Rev.*, 2021, 11614–11667.
90 B. Freis, G. Cotin, F. Perton, D. Mertz, S. Boutry, S. Laurent and S. Begin-Colin, *The Size, Shape, and Composition Design of Iron Oxide Nanoparticles to Combine, MRI, Magnetic Hyperthermia, and Photothermia*, 2021.
91 F. Canfarotta and S. A. Piletsky, *Adv. Healthcare Mater.*, 2014, **3**, 160–175.
92 P. Kucheryavy, J. He, V. T. John, P. Maharjan, L. Spinu, G. Z. Goloverda and V. L. Kolesnichenko, *Langmuir*, 2013, **29**, 710–716.
93 U. I. Tromsdorf, O. T. Bruns, S. C. Salmen, U. Beisiegel and H. Weller, *Nano Lett.*, 2009, **9**, 4434–4440.
94 S. Tong, S. Hou, Z. Zheng, J. Zhou and G. Bao, *Nano Lett.*, 2010, **10**, 4607–4613.
95 Z. Zhou, L. Wang, X. Chi, J. Bao, L. Yang, W. Zhao, Z. Chen, X. Wang, X. Chen and J. Gao, *ACS Nano*, 2013, **7**, 3287–3296.
96 J. Y. Park, M. J. Baek, E. S. Choi, S. Woo, J. H. Kim, T. J. Kim, J. C. Jung, K. S. Chae, Y. Chang and G. H. Lee, *ACS Nano*, 2009, **3**, 3663–3669.
97 M. E. Caldorera-Moore, W. B. Liechty and N. A. Peppas, *Acc. Chem. Res.*, 2011, **44**, 1061–1070.
98 S. Fu, Z. Cai and H. Ai, *Adv. Healthcare Mater.*, 2021, **10**, 2001091.
99 L. M. Ferreira, *Exp. Mol. Pathol.*, 2010, **89**, 372–380.
100 E. D. Smolensky, H.-Y. E. Park, Y. Zhou, G. A. Rolla, M. Marjańska, M. Botta and V. C. Pierre, *J. Mater. Chem. B*, 2013, **1**, 2818–2828.
101 G. Wang, X. Zhang, A. Skallberg, Y. Liu, Z. Hu, X. Mei and K. Uvdal, *Nanoscale*, 2014, **6**, 2953–2963.
102 P. Caravan, C. T. Farrar, L. Frullano and R. Uppal, *Contrast Media Mol. Imaging*, 2009, **4**, 89–100.
103 J. Schubert and M. Chanana, *Curr. Med. Chem.*, 2018, **25**, 4553–4586.
104 A. Neuwelt, N. Sidhu, C.-A. A. Hu, G. Mlady, S. C. Eberhardt and L. O. Sillerud, *Am. J. Roentgenol.*, 2015, **204**, W302–W313.
105 J. Lodhia, G. Mandarano, N. Ferris, P. Eu and S. Cowell, *Biomed. Imaging Intervention J.*, 2010, **6**, e12.
106 J. Dulińska-Litewka, A. Łazarczyk, P. Hałubiec, O. Szafrański, K. Karnas and A. Karewicz, *Materials*, 2019, **12**, 617.
107 S. Yoffe, T. Leshuk, P. Everett and F. Gu, *Curr. Pharm. Des.*, 2013, **19**, 493–509.
108 R. Singh and J. W. Lillard Jr, *Exp. Mol. Pathol.*, 2009, **86**, 215–223.
109 S. Laurent, A. A. Saei, S. Behzadi, A. Panahifar and M. Mahmoudi, *Expert Opin. Drug Delivery*, 2014, **11**, 1449–1470.
110 J. Nowak-Jary and B. Machnicka, *Int. J. Nanomed.*, 2023, 4067–4100.
111 N. Singh, G. J. Jenkins, R. Asadi and S. H. Doak, *Nano Rev.*, 2010, **1**, 5358.
112 M. Longmire, P. L. Choyke and H. Kobayashi, *Nanomedicine*, 2008, **3**, 703–717.
113 X. Wang, L. Yang, Z. Chen and D. M. Shin, *Ca-Cancer J. Clin.*, 2008, **58**, 97–110.
114 R. Thomas, I.-K. Park and Y. Y. Jeong, *Int. J. Mol. Sci.*, 2013, **14**, 15910–15930.
115 A. Parmanik, A. Bose and B. Ghosh, *Minerva Biotechnol. Biomol.*, 2022, **34**, 86.

116 S. Laurent, D. Forge, M. Port, A. Roch, C. Robic, L. Vander Elst and R. N. Muller, *Chem. Rev.*, 2008, **108**, 2064–2110.
117 M. K. Yu, J. Park, Y. Y. Jeong, W. K. Moon and S. Jon, *Nanotechnology*, 2010, **21**, 415102.
118 G. B. Chavhan, P. S. Babyn, B. Thomas, M. M. Shroff and E. M. Haacke, *Radiographics*, 2009, **29**, 1433–1449.
119 J. Zhang, R. Chamberlain, M. Etheridge, D. Idiyatullin, C. Corum, J. Bischof and M. Garwood, *Magn. Reson. Med.*, 2014, **71**, 1982–1988.
120 O. M. Girard, J. Du, L. Agemy, K. N. Sugahara, V. R. Kotamraju, E. Ruoslahti, G. M. Bydder and R. F. Mattrey, *Magn. Reson. Med.*, 2011, **65**, 1649–1660.
121 Y.-N. Zhang, W. Poon, A. J. Tavares, I. D. McGilvray and W. C. Chan, *J. Controlled Release*, 2016, **240**, 332–348.
122 Y.-X. J. Wang, S. M. Hussain and G. P. Krestin, *Eur. Radiol.*, 2001, **11**, 2319–2331.
123 H. L. Ma, Y. F. Xu, X. R. Qi, Y. Maitani and T. Nagai, *Int. J. Pharm.*, 2008, **354**, 217–226.
124 Z. Bakhtiary, A. A. Saei, M. J. Hajipour, M. Raoufi, O. Vermesh and M. Mahmoudi, *Nanomed. Nanotechnol. Biol. Med.*, 2016, **12**, 287–307.
125 X. Duan and Y. Li, *Small*, 2013, **9**, 1521–1532.
126 A. S. Karakoti, S. Das, S. Thevuthasan and S. Seal, *Angew. Chem., Int. Ed.*, 2011, **50**, 1980–1994.
127 A. Albanese, P. S. Tang and W. C. Chan, *Annu. Rev. Biomed. Eng.*, 2012, **14**, 1–16.
128 D. Bobo, K. J. Robinson, J. Islam, K. J. Thurecht and S. R. Corrie, *Pharm. Res.*, 2016, **33**, 2373–2387.
129 B. Thapa, D. Diaz-Diestra, J. Beltran-Huarac, B. R. Weiner and G. Morell, *Nanoscale Res. Lett.*, 2017, **12**, 1–13.
130 R. Canese, F. Vurro and P. Marzola, *Nanomaterials*, 2021, **11**, 1950.
131 H. Yang, H. Wang, C. Wen, S. Bai, P. Wei, B. Xu, Y. Xu, C. Liang, Y. Zhang and G. Zhang, *J. Nanobiotechnol.*, 2022, **20**, 98.
132 M. Stuber, W. D. Gilson, M. Schär, D. A. Kedziorek, L. V. Hofmann, S. Shah, E. J. Vonken, J. W. M. Bulte and D. L. Kraitchman, *Magn. Reson. Med.*, 2007, **58**, 1072–1077.
133 L. Han, Y. Zhang, Y. Zhang, Y. Shu, X.-W. Chen and J.-H. Wang, *Talanta*, 2017, **171**, 32–38.
134 Q. Zhang, W. Shan, C. Ai, Z. Chen, T. Zhou, X. Lv, X. Zhou, S. Ye, L. Ren and X. Wang, *Nanotheranostics*, 2018, **2**, 87–95.
135 H. Yang, Y. Chen, Z. Chen, Y. Geng, X. Xie, X. Shen, T. Li, S. Li, C. Wu and Y. Liu, *Biomater. Sci.*, 2017, **5**, 1001–1013.
136 Y. Zeng, L. Wang, Z. Zhou, X. Wang, Y. Zhang, J. Wang, P. Mi, G. Liu and L. Zhou, *Biomater. Sci.*, 2017, **5**, 50–56.
137 C. Wang, N. Zhao, Y. Huang, R. He, S. Xu and W. Yuan, *Chem. Eng. J.*, 2020, **401**, 126100.
138 D. Yan, X. Liu, G. Deng, H. Yuan, Q. Wang, L. Zhang and J. Lu, *J. Colloid Interface Sci.*, 2018, **530**, 547–555.
139 D. Zhong, J. Zhao, Y. Li, Y. Qiao, Q. Wei, J. He, T. Xie, W. Li and M. Zhou, *Biomaterials*, 2019, **219**, 119369.
140 X. Shen, T. Li, Z. Chen, Y. Geng, X. Xie, S. Li, H. Yang, C. Wu and Y. J. I. j. o. n. Liu, *Int. J. Nanomed.*, 2017, **12**, 4299.
141 T. Zhu, X. Ma, R. Chen, Z. Ge, J. Xu, X. Shen, L. Jia, T. Zhou, Y. Luo and T. Ma, *Biomater. Sci.*, 2017, **5**, 1090–1100.
142 M. Gorgizadeh, N. Azarpira, M. Lotfi, F. Daneshvar, F. Salehi and N. Sattarahmady, *Photodiagn. Photodyn. Ther.*, 2019, **27**, 27–33.
143 H. Zhang, Y.-H. Li, Y. Chen, M.-M. Wang, X.-S. Wang and X.-B. Yin, *Sci. Rep.*, 2017, **7**, 44153.
144 G. Yang, R. Zhang, C. Liang, H. Zhao, X. Yi, S. Shen, K. Yang, L. Cheng and Z. Liu, *Small*, 2018, **14**, 1702664.
145 F. Wang, L. Wen, J. Liu, W. Peng, Z. Meng, Q. Chen, Y. Wang, B. Ke, Y. Guo and P. Mi, *Biomaterials*, 2020, **230**, 119614.
146 W. Fang, W. Zhu, H. Chen, H. Zhang, S. Hong, W. Wei and T. Zhao, *ACS Appl. Bio Mater.*, 2020, **3**, 1690–1697.
147 H. Guo, X. Zhao, H. Sun, H. Zhu and H. Sun, *Nanotechnology*, 2018, **30**, 075101.
148 K. Liang, Z. Li, Y. Luo, Q. Zhang, F. Yin, L. Xu, H. Chen and H. Wang, *Small*, 2020, **16**, 1906985.
149 Z. Yang, J. Ren, Z. Ye, W. Zhu, L. Xiao, L. Zhang, Q. He, Z. Xu and H. Xu, *J. Mater. Chem. B*, 2017, **5**, 1108–1116.
150 P. Xie, P. Du, J. Li and P. Liu, *Carbohydr. Polym.*, 2019, **205**, 377–384.
151 M. G. Adimoolam, N. Amreddy, M. R. Nalam and M. V. Sunkara, *J. Magn. Magn. Mater.*, 2018, **448**, 199–207.
152 G. J. Strijkers, W. J. M Mulder, G. A. F van Tilborg and K. Nicolay, *Anti-Cancer Agents Med. Chem.*, 2007, **7**, 291–305.
153 A. Taylor, K. M. Wilson, P. Murray, D. G. Fernig and R. Levy, *Chem. Soc. Rev.*, 2012, **41**, 2707–2717.
154 L. Zhao, R. Chen, F. Li, L. Yang, J. Peng, J. Li, H. Xiang, H. P. Tham, H. Chen, Y. Su, Y. Zhao, P. Xing, W. Yuan and W. Q. Lim, *Adv. Funct. Mater.*, 2018, **28**, 1806162.
155 L. Meng, Y. Lu, Y. Lu, H. Xu, G. Sheng, F. Han, Z. Wu, C. Han, C. Wang and L. Yang, *ACS Appl. Mater. Interfaces*, 2021, **13**, 11657–11671.
156 H. Y. Tanaka, A. Enomoto, A. Masamune, T. Nakazawa and M. R. Kano, *Cancers*, 2023, **15**, 724.
157 B. J. Boyd, A. Galle, M. Daglas, J. V. Rosenfeld and R. Medcalf, *J. Drug Targeting*, 2015, **23**, 847–853.
158 M. Zhang, H. Cong, H. Ma, X. Wang, B. Yu and Y. Shen, *J. Controlled Release*, 2023, **354**, 167–187.
159 Z. Mi, J. Zheng, J. Liu, Z. Liu, H. Tan, W. Zhou, X. Ma, P. Rong, Q. Yao and Y. Qi, *Acta Pharm. Sin. B*, 2023, **13**, 819–833.
160 Y.-w. Jun, Y.-M. Huh, J.-s. Choi, J.-H. Lee, H.-T. Song, S. Kim, S. Yoon, K.-S. Kim, J.-S. Shin and J.-S. Suh, *J. Am. Chem. Soc.*, 2005, **127**, 5732–5733.
161 M. E. Lorkowski, P. U. Atukorale, K. B. Ghaghada and E. Karathanasis, *Adv. Healthcare Mater.*, 2021, **10**, 2001044.
162 P. Moroz, C. Metcalf and B. N. Gray, *BioMetals*, 2003, **16**, 455–464.
163 H. M. Joshi, Y. P. Lin, M. Aslam, P. Prasad, E. A. Schultz-Sikma, R. Edelman, T. Meade and V. P. Dravid, *J. Phys. Chem. C*, 2009, **113**, 17761–17767.
164 C. Bárcena, A. K. Sra, G. S. Chaubey, C. Khemtong, J. P. Liu and J. Gao, *Chem. Commun.*, 2008, 2224–2226.
165 J. t. Jang, H. Nah, J. H. Lee, S. H. Moon, M. G. Kim and J. Cheon, *Angew. Chem., Int. Ed.*, 2009, **48**, 1234–1238.
166 P. Zhang, Y. Hou, J. Zeng, Y. Li, Z. Wang, R. Zhu, T. Ma and M. Gao, *Angew. Chem.*, 2019, **58**, 11088–11096.

167 M. H. Safdar, Z. Hussain, M. A. Abourehab, H. Hasan, S. Afzal and H. E. Thu, *Artif. Cells, Nanomed., Biotechnol.*, 2018, **46**, 1967–1980.

168 M. Mahmoudi, S. Sant, B. Wang, S. Laurent and T. Sen, *Adv. Drug Delivery Rev.*, 2011, **63**, 24–46.

169 E. Kianfar, *J. Supercond. Novel Magn.*, 2021, **34**, 1709–1735.

170 L. Shen, B. Li and Y. Qiao, *Materials*, 2018, **11**, 324.

171 W. H. De Jong and P. J. A. Borm, *Int. J. Nanomed.*, 2008, **3**, 133–149.

172 A. Ali, H. Zafar, M. Zia, I. Ul Haq, A. R. Phull, J. S. Ali and A. Hussain, *Nanotechnol., Sci. Appl.*, 2016, **9**, 49–67.

173 M. Arruebo, R. Fernández-Pacheco, M. R. Ibarra and J. Santamaría, *Nano Today*, 2007, **2**, 22–32.

174 F. Assa, H. Jafarizadeh-Malmiri, H. Ajamein, H. Vaghari, N. Anarjan, O. Ahmadi and A. Berenjian, *Crit. Rev. Biotechnol.*, 2017, **37**, 492–509.

175 J. K. Patra, G. Das, L. F. Fraceto, E. V. R. Campos, M. D. P. Rodriguez-Torres, L. S. Acosta-Torres, L. A. Diaz-Torres, R. Grillo, M. K. Swamy, S. Sharma, S. Habtemariam and H.-S. Shin, *J. Nanobiotechnol.*, 2018, **16**, 71.

176 A. Ali, M. Z. Hira Zafar, I. ul Haq, A. R. Phull, J. S. Ali and A. Hussain, *Nanotechnol., Sci. Appl.*, 2016, **9**, 49.

177 S. D. Anderson, V. V. Gwenin and C. D. Gwenin, *Nanoscale Res. Lett.*, 2019, **14**, 188.

178 J.-E. Kim, J.-Y. Shin and M.-H. Cho, *Arch. Toxicol.*, 2012, **86**, 685–700.

179 C. Gao, Q. Huang, C. Liu, C. H. Kwong, L. Yue, J.-B. Wan, S. M. Lee and R. Wang, *Nat. Commun.*, 2020, **11**, 1–14.

180 S. O. Aisida, P. A. Akpa, I. Ahmad, T.-k. Zhao, M. Maaza and F. I. Ezema, *Eur. Polym. J.*, 2020, **122**, 109371.

181 A. T. Thodikayil, S. Sharma and S. Saha, *ACS Appl. Bio Mater.*, 2021, **4**, 2907–2940.

182 A. Sionkowska, *Prog. Polym. Sci.*, 2011, **36**, 1254–1276.

183 C. Englert, J. C. Brendel, T. C. Majdanski, T. Yildirim, S. Schubert, M. Gottschaldt, N. Windhab and U. S. Schubert, *Prog. Polym. Sci.*, 2018, **87**, 107–164.

184 S. Natarajan, K. Harini, G. P. Gajula, B. Sarmento, M. T. Neves-Petersen and V. Thiagarajan, *BMC Mater.*, 2019, **1**, 1–22.

185 C. Combes and C. Rey, *Acta Biomater.*, 2010, **6**, 3362–3378.

186 S. Gurunathan, M.-H. Kang, M. Qasim and J.-H. Kim, *Int. J. Mol. Sci.*, 2018, **19**, 3264.

187 V. F. Cardoso, A. Francesko, C. Ribeiro, M. Bañobre-López, P. Martins and S. Lanceros-Mendez, *Adv. Healthcare Mater.*, 2018, **7**, 1700845.

188 L. H. Reddy, J. L. Arias, J. Nicolas and P. Couvreur, *Chem. Rev.*, 2012, **112**, 5818–5878.

189 N. K. Jain, P. R. S, M. C. Bavya, R. Prasad, R. Bandyopadhyaya, V. G. M. Naidu and R. Srivastava, *RSC Adv.*, 2019, **9**, 26572–26581.

190 K. Turcheniuk, A. V. Tarasevych, V. P. Kukhar, R. Boukherroub and S. Szunerits, *Nanoscale*, 2013, **5**, 10729–10752.

191 R. Cagliani, F. Gatto and G. Bardi, *Materials*, 2019, **12**, 1991.

192 D. E. Owens III and N. A. Peppas, *Int. J. Pharm.*, 2006, **307**, 93–102.

193 N. Erathodiyil and J. Y. Ying, *Acc. Chem. Res.*, 2011, **44**, 925–935.

194 Y. Chen, K. Ai, J. Liu, G. Sun, Q. Yin and L. Lu, *Biomaterials*, 2015, **60**, 111–120.

195 S. Wilhelm, A. J. Tavares, Q. Dai, S. Ohta, J. Audet, H. F. Dvorak and W. C. Chan, *Nat. Rev. Mater.*, 2016, **1**, 1–12.

196 C. Sun, J. S. Lee and M. Zhang, *Adv. Drug Delivery Rev.*, 2008, **60**, 1252–1265.

197 Y. Zhu, J. Li, W. Li, Y. Zhang, X. Yang, N. Chen, Y. Sun, Y. Zhao, C. Fan and Q. Huang, *Theranostics*, 2012, **2**, 302.

198 A. S. Lübbe, C. Alexiou and C. Bergemann, *J. Surg. Res.*, 2001, **95**, 200–206.

199 O. Rotariu and N. J. C. Strachan, *J. Magn. Magn. Mater.*, 2005, **293**, 639–646.

200 K. T. Al-Jamal, J. Bai, J. T.-W. Wang, A. Protti, P. Southern, L. Bogart, H. Heidari, X. Li, A. Cakebread and D. Asker, *Nano Lett.*, 2016, **16**, 5652–5660.

201 C. Alexiou, D. Diehl, P. Henninger, H. Iro, R. Rockelein, W. Schmidt and H. Weber, *IEEE Trans. Appl. Supercond.*, 2006, **16**, 1527–1530.

202 J. Estelrich, E. Escribano, J. Queralt and M. A. Busquets, *Int. J. Mol. Sci.*, 2015, **16**, 8070–8101.

203 B. Gleich, N. Hellwig, H. Mannell, R. Jurgons, C. Seliger, C. Alexiou, B. Wolf and T. Weyh, *IEEE Trans. Nanotechnol.*, 2007, **6**, 164–170.

204 R. Krzyminiewski, B. Dobosz, G. Schroeder and J. Kurczewska, *Phys. Lett. A*, 2018, **382**, 3192–3196.

205 A. Hajiaghajani and A. Abdolali, *Bioelectromagnetics*, 2018, **39**, 325–338.

206 C. Corot, P. Robert, J.-M. Idée and M. Port, *Adv. Drug Delivery Rev.*, 2006, **58**, 1471–1504.

207 Z. Hedayatnasab, F. Abnisa and W. M. A. W. Daud, *Mater. Des.*, 2017, **123**, 174–196.

208 E. Guisasola, L. Asín, L. Beola, J. M. de la Fuente, A. Baeza and M. Vallet-Regí, *ACS Appl. Mater. Interfaces*, 2018, **10**, 12518–12525.

209 M. Das, A. Solanki, A. Joshi, R. Devkar, S. Seshadri and S. Thakore, *Carbohydr. Polym.*, 2019, **206**, 694–705.

210 X. Liu, M. D. Kaminski, H. Chen, M. Torno, L. Taylor and A. J. Rosengart, *J. Controlled Release*, 2007, **119**, 52–58.

211 F. Hu, K. Neoh and E. Kang, *Biomaterials*, 2006, **27**, 5725–5733.

212 J. L. Arias, M. A. Ruiz, V. Gallardo and Á. V. Delgado, *J. Controlled Release*, 2008, **125**, 50–58.

213 S. Ayyanaar, M. P. Kesavan, C. Balachandran, S. Rasala, P. Rameshkumar, S. Aoki, J. Rajesh, T. J. Webster and G. Rajagopal, *Nanomed. Nanotechnol. Biol. Med.*, 2020, **24**, 102134.

214 A. Amani, J. M. Begdelo, H. Yaghoubi and S. Motallebinia, *J. Drug Delivery Sci. Technol.*, 2019, **49**, 534–546.

215 T. Haider, V. Pandey, C. Behera, P. Kumar, P. N. Gupta and V. Soni, *J. Drug Delivery Sci. Technol.*, 2020, **60**, 102087.

216 A. Seyfoori, S. A. S. Ebrahimi, S. Omidian and S. M. Naghib, *J. Taiwan Inst. Chem. Eng.*, 2019, **96**, 503–508.

217 Y. Ding, Y. Hu, L. Zhang, Y. Chen and X. Jiang, *Biomacromolecule*, 2006, **7**, 1766–1772.

218 N. S. Elbialy, M. M. Fathy and W. M. Khalil, *Int. J. Pharm.*, 2015, **490**, 190–199.

219 T. T. Hoang Thi, D.-H. Nguyen Tran, L. G. Bach, H. Vu-Quang, D. C. Nguyen, K. D. Park and D. H. Nguyen, *Pharmaceutics*, 2019, **11**, 120.

220 S. Patra, E. Roy, P. Karfa, S. Kumar, R. Madhuri and P. K. Sharma, *ACS Appl. Mater. Interfaces*, 2015, **7**, 9235–9246.

221 M. Satpathy, L. Wang, R. J. Zielinski, W. Qian, Y. A. Wang, A. M. Mohs, B. A. Kairdolf, X. Ji, J. Capala, M. Lipowska, S. Nie, H. Mao and L. Yang, *Theranostics*, 2019, **9**, 778–795.

222 M. Sun, X. Fan, X. Meng, J. Song, W. Chen, L. Sun and H. Xie, *Nanoscale*, 2019, **11**, 18382–18392.

223 S. Senapati, R. Shukla, Y. B. Tripathi, A. K. Mahanta, D. Rana and P. Maiti, *Mol. Pharmaceutics*, 2018, **15**, 679–694.

224 I. Dagogo-Jack and A. T. Shaw, *Nat. Rev. Clin. Oncol.*, 2018, **15**, 81–94.

225 T. B. Huff, L. Tong, Y. Zhao, M. N. Hansen, J. X. Cheng and A. Wei, *Nanomedicine*, 2007, **2**, 125–132.

226 P. Kaur, M. D. Hurwitz, S. Krishnan and A. Asea, *Cancers*, 2011, **3**, 3799–3823.

227 Q. Zhou, J. Li, J. Xiang, S. Shao, Z. Zhou, J. Tang and Y. Shen, *Adv. Drug Delivery Rev.*, 2022, **189**, 114480.

228 J. D. Urbano-Gámez, C. Guzzi, M. Bernal, J. Solivera, I. Martínez-Zubiaurre, C. Caro and M. L. García-Martín, *Int. J. Mol. Sci.*, 2024, **25**, 5213.

229 M. J. Molaei, *J. Biomater. Appl.*, 2024, **39**, 3–23.

230 A. Gholami, S. M. Mousavi, S. A. Hashemi, Y. Ghasemi, W.-H. Chiang and N. Parvin, *Drug Metab. Rev.*, 2020, **52**, 205–224.

231 Y. Chen, T. Wang, X. Liu, Y. Wang, M. Lu and J. Cao, *Nanoscale Res. Lett.*, 2016, **11**, 1–6.

232 M. Häring, J. Mayr, S. Grijalvo, J. Schiller, R. Eritja and D. Díaz, *Gels*, 2015, **1**, 135–161.

233 K. Maier-Hauff, R. Rothe, R. Scholz, U. Gneveckow, P. Wust, B. Thiesen, A. Feussner, A. von Deimling, N. Waldoefner, R. Felix and A. Jordan, *J. Neurooncol.*, 2007, **81**, 53–60.

234 H. A. Albarqi, A. S. Moses, M. N. Hansen, P. Dhagat, A. A. Demessie, F. Y. Sabei, O. Taratula and O. R. Taratula, *Pharmaceutics*, 2020, **12**, 1020.

235 H. A. Albarqi, T. Korzun, A. S. Moses, M. N. Hansen, L. H. Wong, O. Taratula, P. Dhagat, F. Y. Sabei, O. Taratula, X. Li and C. Schumann, *ACS Nano*, 2019, **13**, 6383–6395.

236 C. Caro, J. M. Paez-Muñoz, M. Pernía Leal, M. Carayol, M. Feijoo-Cuaresma and M. L. García-Martín, *Adv. Healthcare Mater.*, 2025, **14**, 2404391.

237 D. Kong, X. Zheng, K. Ding, R. Zhong, Z. Zhang, Q. Wang, C. Dong, Z. Zheng, X. Li and J. Weng, *Adv. Healthcare Mater.*, 2025, **14**, 2401749.

238 S. Pathak, *RMIT University*: Melbourne, Australia, 2020.

239 J. Iqbal, S. Maqbool and N. Bhatti, in *Magnetic Polymer Composites and Their Emerging Applications*, CRC Press, 2024, pp. 39–67.

240 V. Ghai, S. Pandit, M. Svensso, R. Larsson, A. Matic, R. Ngaloy, S. P. Dash, A. Terry, K. Nygård and I. Mijakovic, *Adv. Funct. Mater.*, 2024, **34**, 2406875.

241 Z. Zhao, J. Zhao, J. Qin, Y. Sun, W. Xia, Z. Chao, R. Chen, A. Yan and L. Jiang, *Scr. Mater.*, 2024, **245**, 116056.

242 A. Hervault and N. T. K. Thanh, *Nanoscale*, 2014, **6**, 11553–11573.

243 Y. Javed, K. Ali and Y. Jamil, in *Complex Magnetic Nanostructures: Synthesis, Assembly and Applications*, ed. S. K. Sharma, Springer International Publishing, Cham, 2017, pp. 393–424, DOI: 10.1007/978-3-319-52087-2_11.

244 X. Liu, Y. Zhang, Y. Wang, W. Zhu, G. Li, X. Ma, Y. Zhang, S. Chen, S. Tiwari and K. Shi, *Theranostics*, 2020, **10**, 3793.

245 H. Kurebayashi, J. H. Garcia, S. Khan, J. Sinova and S. Roche, *Nat. Rev. Phys.*, 2022, **4**, 150–166.

246 V. V. Mody, A. Singh and B. Wesley, *Eur. J. Nanomed.*, 2013, **5**, 11.

247 N. A. De Oliveira and P. J. von Ranke, *Phys. Rep.*, 2010, **489**, 89–159.

248 A. Kolhatkar, R. Willson, D. Litvinov, T. Lee and A. Jamison, *Int. J. Mol. Sci.*, 2013, **14**, 15977–16009.

249 S. K. Pal, C. Frommen, S. Kumar, B. C. Hauback, H. Fjellvåg and G. Helgesen, *Mater. Des.*, 2020, **195**, 109036.

250 A. E. Deatsch and B. A. Evans, *J. Magn. Magn. Mater.*, 2014, **354**, 163–172.

251 E. Esmaeili, R. Ghazanfar Chaydareh and S. A. Rounaghi, *Appl. Therm. Eng.*, 2017, **110**, 1212–1219.

252 S. Ota and Y. Takemura, *J. Phys. Chem. C*, 2019, **123**, 28859–28866.

253 D. Chang, M. Lim, J. A. Goos, R. Qiao, Y. Y. Ng, F. M. Mansfeld, M. Jackson, T. P. Davis and M. Kavallaris, *Front. Pharmacol*, 2018, **9**, 831.

254 H. A. Albarqi, L. H. Wong, C. Schumann, F. Y. Sabei, T. Korzun, X. Li, M. N. Hansen, P. Dhagat, A. S. Moses and O. Taratula, *ACS Nano*, 2019, **13**, 6383–6395.

255 V. V. Mody, A. Singh and B. Wesley, *Eur. J. Nanomed.*, 2013, **5**, 11–21.

256 R. Hergt, R. Hiergeist, M. Zeisberger, G. Glöckl, W. Weitschies, L. P. Ramirez, I. Hilger and W. A. Kaiser, *J. Magn. Magn. Mater.*, 2004, **280**, 358–368.

257 M. Kallumadil, M. Tada, T. Nakagawa, M. Abe, P. Southern and Q. A. Pankhurst, *J. Magn. Magn. Mater.*, 2009, **321**, 1509–1513.

258 K. Hadian and B. R. Stockwell, *Nat. Rev. Drug Discovery*, 2023, **22**, 723–742.

259 V. Vilas-Boas, F. Carvalho and B. Espiña, *Molecules*, 2020, **25**, 2874.

260 G. Bergers and S.-M. Fendt, *Nat. Rev. Cancer*, 2021, **21**, 162–180.

261 M. Cohen-Erner, R. Khandadash, R. Hof, O. Shalev, A. Antebi, A. Cyjon, D. Kanakov, A. Nyska, G. Goss and J. Hilton, *ACS Appl. Nano Mater.*, 2021, **4**, 11187–11198.

262 A. Seynhaeve, M. Amin, D. Haemmerich, G. Van Rhoon and T. Ten Hagen, *Adv. Drug Delivery Rev.*, 2020, **163**, 125–144.

263 E. Myrovali, N. Maniotis, T. Samaras and M. Angelakeris, *Nanoscale Adv.*, 2020, **2**, 408–416.

264 I. M. Obaidat, V. Narayanaswamy, S. Alaabed, S. Sambasivam and C. V. Muralee Gopi, *Magnetochemistry*, 2019, **5**, 67.

265 I. M. Obaidat, B. Issa and Y. Haik, *Nanomaterials*, 2015, **5**, 63–89.

266 C. Martinez-Boubeta, K. Simeonidis, A. Makridis, M. Angelakeris, O. Iglesias, P. Guardia, A. Cabot, L. Yedra, S. Estradé, F. Peiró, Z. Saghi, P. A. Midgley, I. Conde-Leborán, D. Serantes and D. Baldomir, *Sci. Rep.*, 2013, **3**, 1652.

267 Y.-w. Jun, J.-w. Seo and J. Cheon, *Acc. Chem. Res.*, 2008, **41**, 179–189.

268 R. E. Rosensweig, *J. Magn. Magn. Mater.*, 2002, **252**, 370–374.

269 E. J. Lee, N. K. Lee, Y. Yang, E. Koh, G. H. Nam, C. Jeong, S. Y. Park, I. S. Kim, S. Kim, Y. K. Kim, M. Kih and Y. Hong, *Adv. Mater.*, 2018, **30**, 1705581.

270 M. Barrow, A. Taylor, P. Murray, M. J. Rosseinsky and D. J. Adams, *Chem. Soc. Rev.*, 2015, **44**, 6733–6748.

271 M. Smit, PhD thesis, Stellenbosch University, Stellenbosch, 2022.

272 K. Simeonidis, C. Martinez-Boubeta, D. Serantes, S. Ruta, O. Chubykalo-Fesenko, R. Chantrell, J. Oró-Solé, L. Balcells, A. S. Kamzin, R. A. Nazipov, A. Makridis and M. Angelakeris, *ACS Appl. Nano Mater.*, 2020, **3**, 4465–4476.

273 Y. Wang, L. Zou, Z. Qiang, J. Jiang, Z. Zhu and J. Ren, *ACS Biomater. Sci. Eng.*, 2020, **6**, 3550–3562.

274 K. Loizou, S. Mourdikoudis, A. Sergides, M. O. Besenhard, C. Sarafidis, K. Higashimine, O. Kalogirou, S. Maenosono, N. T. K. Thanh and A. Gavriilidis, *ACS Appl. Mater. Interfaces*, 2020, **12**, 28520–28531.

275 H. Etemadi and P. G. Plieger, *ACS Omega*, 2020, **5**, 18091–18104.

276 P. Kowalik, J. Mikulski, A. Borodziuk, M. Duda, I. Kamińska, K. Zajdel, J. Rybusinski, J. Szczytko, T. Wojciechowski, K. Sobczak, R. Minikayev, M. Kulpa-Greszta, R. Pazik, P. Grzaczkowska, K. Fronc, M. Lapinski, M. Frontczak-Baniewicz and B. Sikora, *J. Phys. Chem. C*, 2020, **124**, 6871–6883.

277 L. B. de Mello, L. C. Varanda, F. A. Sigoli and I. O. Mazali, *J. Alloys Compd.*, 2019, **779**, 698–705.

278 S. Liébana-Viñas, K. Simeonidis, U. Wiedwald, Z. A. Li, Z. Ma, E. Myrovali, A. Makridis, D. Sakellari, G. Vourlias, M. Spasova, M. Farle and M. Angelakeris, *RSC Adv.*, 2016, **6**, 72918–72925.

279 D. Lachowicz, W. Górka, A. Kmita, A. Bernasik, J. Żukrowski, W. Szczerba, M. Sikora, C. Kapusta and S. Zapotoczny, *J. Mater. Chem. B*, 2019, **7**, 2962–2973.

280 C. Virlan, G. Bulai, O. F. Caltun, R. Hempelmann and A. Pui, *Ceram. Int.*, 2016, **42**, 11958–11965.

281 S. G. Mendo, A. F. Alves, L. P. Ferreira, M. M. Cruz, M. H. Mendonça, M. Godinho and M. D. Carvalho, *New J. Chem.*, 2015, **39**, 7182–7193.

282 E. Fantechi, C. Innocenti, M. Albino, E. Lottini and C. Sangregorio, *J. Magn. Magn. Mater.*, 2015, **380**, 365–371.

283 P. H. Nam, L. T. Lu, P. H. Linh, D. H. Manh, L. T. Thanh Tam, N. X. Phuc, P. T. Phong and I.-J. Lee, *New J. Chem.*, 2018, **42**, 14530–14541.

284 A. Pardo, B. Pelaz, J. Gallo, M. Bañobre-López, W. J. Parak, S. Barbosa, P. del Pino and P. Taboada, *Chem. Mater.*, 2020, **32**, 2220–2231.

285 M. Albino, E. Fantechi, C. Innocenti, A. López-Ortega, V. Bonanni, G. Campo, F. Pineider, M. Gurioli, P. Arosio and T. Orlando, *J. Phys. Chem. C*, 2019, **123**, 6148–6157.

286 S. Jadhav, P. Shewale, B. Shin, M. Patil, G. Kim, A. Rokade, S. Park, R. Bohara and Y. Yu, *J. Colloid Interface Sci.*, 2019, **541**, 192–203.

287 E. Cheraghipour, S. Javadpour and A. R. Mehdizadeh, *J. Biomed. Eng.*, 2012, **5**, 715–719.

288 V. Mameli, A. Musinu, A. Ardu, G. Ennas, D. Peddis, D. Niznansky, C. Sangregorio, C. Innocenti, N. T. Thanh and C. Cannas, *Nanoscale*, 2016, **8**, 10124–10137.

289 Z. Nemati, S. Salili, J. Alonso, A. Ataie, R. Das, M. Phan and H. Srikanth, *J. Alloys Compd.*, 2017, **714**, 709–714.

290 A. S. Garanina, A. G. Majouga, T. O. Abakumova, A. O. Prelovskaya, A. S. Semkina, P. V. Gorelkin, A. A. Nikitin, V. A. Naumenko, A. S. Erofeev, M. A. Abakumov and U. Wiedwald, *Nanomaterials*, 2021, **12**, 38.

291 P. B. Balakrishnan, S. Fernandes, M. Miscuglio, S. Ruta, D. Serantes, T. Pellegrino, N. Silvestri, O. Hovorka, R. Chantrell, K. Livesey, S. Fiorito, T. Fernandez-Cabada and F. Marinaro, *Adv. Mater.*, 2020, **32**, 2003712.

292 K. Sule, J. Umbsaar and E. J. Prenner, *Biochim. Biophys. Acta, Biomembr.*, 2020, **1862**, 183250.

293 I. Pereira Gomes, A. L. Chaves Maia, A. L. Branco De Barros, D. Rubello, D. M. Townsend, E. A. Leite and J. Aparecida Duarte, *Pharmaceuticals*, 2019, **12**, 171.

294 X. Ge, R. Wong, A. Anisa and S. Ma, *Biomaterials*, 2021, **281**, 121322.

295 K. Chatterjee, S. Sarkar, K. Jagajjanani Rao and S. Paria, *Adv. Colloid Interface Sci.*, 2014, **209**, 8–39.

296 M. Ravichandran, G. Oza, S. Velumani, J. T. Ramirez, F. Garcia-Sierra, N. B. Andrade, A. Vera, L. Leija and M. A. Garza-Navarro, *Sci. Rep.*, 2016, **6**, 34874.

297 M.-D. Yang, C.-H. Ho, S. Ruta, R. Chantrell, K. Krycka, O. Hovorka, F.-R. Chen, P.-S. Lai and C.-H. Lai, *Adv. Mater.*, 2018, **30**, 1802444.

298 V. Pilati, J. Depeyrot, F. L. O. Paula, P. Coppola, G. F. Goya, F. G. Silva, R. Perzynski, R. Aquino, G. Gomide and R. Cabreira Gomes, *J. Phys. Chem. C*, 2018, **122**, 3028–3038.

299 K. Wu, Y. Chang, S.-H. Liao, N. Suzuki, Y. Yamauchi, B. P. Bastakoti, C.-H. Liu and F.-H. Lin, *Int. J. Nanomed.*, 2015, **10**, 3315.

300 M.-C. Horny, J. Gamby, J.-M. Siaugue and V. Dupuis, *Nanomaterials*, 2021, **11**, 149.

301 P. Takook, M. Persson and H. D. Trefná, *IEEE J. Electromagn. RF Microw. Med. Biol.*, 2018, **2**, 18–24.

302 G. Lassche, J. Crezee and C. M. L. Van Herpen, *Crit. Rev. Oncol./Hematol.*, 2019, **139**, 67–74.

303 X. Wang and L. Cheng, *Nanoscale*, 2019, **11**, 15685–15708.

304 G. Y. Yi, M. J. Kim, H. I. Kim, J. Park and S. H. Baek, *Antioxidants*, 2022, **11**, 625.

305 A. Jordan, R. Scholz, P. Wust, H. Fähling, J. Krause, W. Wlodarczyk, B. Sander, T. Vogl and R. Felix, *Int. J. Hyperthermia*, 1997, **13**, 587–605.